Available online at www.sciencedirect.com
ScienceDirect
European Journal of Mechanics B/Fluids 26 (2007) 305–329

Three-dimensional instabilities of laminar flow in a rough channel and the concept of hydraulically smooth wall

J.M. Floryan

Department of Mechanical and Materials Engineering, The University of Western Ontario, London, Ontario, N6A 5B9, Canada

Received 5 April 2006; received in revised form 7 July 2006; accepted 24 July 2006

Available online 28 August 2006

Abstract

Flow in a channel with distributed surface roughness is considered. Results of the linear stability analysis show that the presence of the roughness destabilizes the traveling-wave instability as well as introduces a new instability that manifests itself in the form of streamwise vortices. The critical conditions for the occurrence of both instabilities are given for different classes of roughness shape. It is shown that these conditions can be predicted with a reasonable accuracy in the case of an arbitrary (but Fourier transformable) roughness by considering only the leading Fourier mode (wavy-wall model). It is argued that the onset of instabilities provides a decision mechanism that determines whether a particular rough wall can be viewed as being hydraulically smooth in the case of transitional flows.

Keywords: Flow instabilities; Distributed surface-roughness; Hydraulically smooth wall

1. Introduction

Flows over rough walls have been studied since the early works of Hagen [1] and Darcy [2], which were focused on turbulent regimes. Reynolds [3] was the first to pose the problem in the context of laminar-turbulent transition. While the questions studied, i.e., what kind of effects the presence of distributed surface roughness can induce in a flow and when a rough wall behaves as hydraulically smooth, are of fundamental importance their rational resolution is still lacking. Both questions are of considerable practical importance in several application areas, e.g., design of large Reynolds number laminar airfoils, small Reynolds number turbulent airfoils, compact heat exchangers, laminar electrostatic precipitators, etc. The original investigations involved measurements of turbulent flows in open channels and in pipes. Various possible roughness forms were classified using the concept of "equivalent roughness" [4]. Phenomenological effects of the "equivalent roughness" were summarized in the form of friction coefficient [5–7]. These and other similar investigations show that surface roughness contributes directly to the dynamics of turbulent flow only if the wall is hydraulically rough. The concept of hydraulic smoothness is very appealing; however, no precise criterion exists for predicting whether a given surface can be considered as being hydraulically smooth for flow conditions of interest. While the modeling concepts of this type have been continuously re-evaluated [8,9], they failed so

E-mail address: mfloryan@eng.uwo.ca (J.M. Floryan).

0997-7546/$ – see front matter
doi:10.1016/j.euromechflu.2006.07.002

far to uncover the mechanisms that govern the complex, flow-condition-dependent interaction between the roughness geometry and the moving fluid.

This work is focused on the determination of the role played by distributed roughness in the laminar-turbulent transition process in shear layers. It is known that this process involves various instabilities that eventually lead to the fully turbulent state. The experimental evidence shows that the roughness contributes directly to the dynamics of the flow only if its amplitude is sufficiently large. A frequently used criterion for determination of the critical roughness size is that the roughness Reynolds number $Re_k = U_k k/\nu < 25$ [10], where k is the roughness height, U_k is the undisturbed velocity at height k and ν the kinematic viscosity. Such a criterion, however, does not address the issue of shape and distribution of the roughness.

There is a large body of experimental observations focused on the laminar-turbulent transition that provide phenomenological description of the flow response in the form of correlations between the height of the roughness, the flow conditions and the critical Reynolds number for certain classes of geometrical forms of the roughness [11–15]. The range of applicability of these correlations is not certain because they are based on a limited experimental data and have been determined for, in essence, artificially created roughness forms. These correlations, nevertheless, form the basis of all roughness sensitive designs.

The surface roughness can be divided into three classes for the purposes of discussion, i.e., isolated two-dimensional roughness, e.g., spanwise trip wire, isolated three-dimensional roughness and distributed roughness. The transition mechanisms for the first class of roughness is associated with inflectional separated velocity profiles and are considered understood at least on qualitative level [16–18]. The characteristic feature of the flow around an isolated, three-dimensional roughness element is the presence of the horseshoe vortex that generates streamwise vortices on the downstream side [10]. The transition mechanism is thought to be associated with the strong instabilities of inflectional shear layers set up by the streamwise vortices, similar to the case of Görtler instability [19]. The effects of distributed roughness are not understood [10]. Various experiments indicate that when the roughness is operative the departure from the laminar state is explosive [20,21]. Theoretical attempts based on the roughness-induced distortion of velocity profile proved inconclusive [22–24] similarly as did concepts based on the roughness-induced additional mixing [25]. The spectral model of roughness shape [26] proved to be very powerful and holds a promise to uncover the mechanisms associated with the distributed roughness. Theoretical analysis of the two-dimensional traveling-wave instability [27] shows that the roughness is responsible for the reduction of the critical Reynolds number and the amount of reduction is in agreement with the experimental observations [28]. Three-dimensional analyses of Couette flow over wavy-wall [29] and Poiseuille flow in a converging-diverging channel [30] show that surface corrugations are able to generate streamwise vortices. Surface roughness may also play a large role in the transition process through amplification of the transient growth mechanism [31]; however, this role remains to be substantiated.

The main objective of this analysis is the determination of the role played by distributed surface roughness in the early stages of the transition process through the use of the linear stability theory. Here we shall follow spectral models [26] where the roughness geometry is represented in terms of Fourier expansions. Analysis of the effects of different geometries is reduced to scans of parameter space formed by the coefficients of such expansions. Use of stability theory provides a convenient tool for the identification of the conditions when the roughness is not hydraulically active; roughness that does not destabilize the flow modifies the flow in an insignificant manner and thus such wall may be considered as hydraulically smooth. The reader should note that the just proposed definition of hydraulic smoothness for transitional flows is different from the common albeit ill-defined smoothness for turbulent flows where the smoothness implies turbulent friction independent of the roughness.

The role of roughness in transitional flows depends on the disturbance level in the flow. The present analysis is focused on the quiet environment where transient growth does not play any role and only disturbances with sustained growth described by the asymptotic instability are able to initiate the transition process. These disturbances include Tollmien–Schlichting (TS) waves, which may be destabilized by the roughness, as well as disturbances in the form of streamwise vortices [29,30] that can be induced by the roughness. We shall attempt to identify conditions when the roughness regardless of its form does not induce any instability and, as a consequence, such a rough wall behaves as hydraulically smooth wall.

The final comment deals with the nomenclature and the term "roughness". This is a conceptual term widely used in the literature and in the discussion above, but nevertheless ill defined. This term only means that the wall is not smooth. In order to be precise, from now on we shall use the term "corrugation" as it implies well defined geometry and, after considering several possible corrugations, we shall inquire if we can generalize our results to arbitrary corrugations

and thus if we can return to the original term, i.e., "roughness". We shall limit our interests to corrugations of small amplitude, as roughness implies small amplitude, and shall consider arbitrary but Fourier transformable shapes.

The analysis is carried out in the context of channel flow where one of the walls is corrugated. The presentation is organized as follows. Section 2 describes steady two-dimensional flow in a channel bounded by a corrugated wall. Section 3 discusses formulation of the linear stability problem relevant to this flow. Section 4 provides discussion of stability properties of the flow for different classes of corrugation shapes. In particular, Section 4.1 deals with the corrugation represented by a single Fourier mode, i.e., wavy-wall model, Section 4.2 considers corrugation in the form of rectangular grooves, Section 4.3 discusses triangular grooves while Section 4.4 considers "sine-bump" grooves. Conditions that guarantee flow stability are given in each case. Comparison of all cases given in Section 5 shows that it is possible to formulate a rational criterion that determines whether a particular wall can be treated as a hydraulically smooth wall. The same section demonstrates generality of the results obtained on the basis of a simple wavy-wall model.

2. Flow in a corrugated channel

In this section, we shall analyze steady, two-dimensional flow in a channel with corrugated lower wall. This presentation is limited to a short outline as details can be found in [26,29]. We begin with the reference plane Poiseuille flow confined between flat rigid walls at $y = \pm 1$ and extending to infinity in the x-direction (Fig. 1). Velocity and pressure fields in the form

$$\mathbf{V}_0(\mathbf{x}) = \big[u_0(y), 0\big] = \big(1 - y^2, 0\big), \qquad p_0(\mathbf{x}) = -2x/Re, \tag{2.1}$$

describe the fluid motion, where the motion is directed towards the positive x-axis, $\mathbf{x} = (x, y)$, and the Reynolds number Re is based on the half-channel height and the maximum x-velocity. Assume that the lower wall is replaced by a corrugated wall whose location $y_L(x)$ is specified as (see Fig. 1)

$$y_L(x) = -1 + \sum_{n=-\infty}^{n=\infty} S^{(n)}\, e^{in\alpha x}, \tag{2.2}$$

where $S^{(n)} = S^{(-n)^*}$ and star denotes the complex conjugate. The wall is characterized by periodicity with the wavelength $\lambda = 2\pi/\alpha$ with the flow domain bounded by $-\infty < x < \infty$, $y_L(x) \leqslant y \leqslant 1$.

The flow in the corrugated channel can be represented as

$$\begin{aligned} &\mathbf{V}_2(\mathbf{x}) = \big[u_2(x, y), v_2(x, y)\big] = \mathbf{V}_0(\mathbf{x}) + \mathbf{V}_1(\mathbf{x}) = \big[u_0(y), 0\big] + \big[u_1(x, y), v_1(x, y)\big], \\ &p_2(\mathbf{x}) = p_0(x) + p_1(x, y), \end{aligned} \tag{2.3}$$

where $\mathbf{V}_1$ and p_1 are the velocity and pressure modifications owing to the presence of the corrugation. Substitution of the above representation of the flow quantities into the Navier–Stokes and continuity equations, introduction of stream

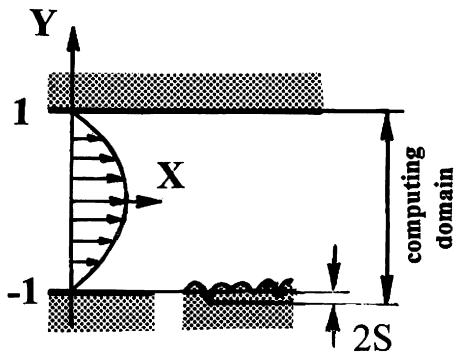

Fig. 1. Sketch of the flow domain. The computational domain is contained between $y = \min(y_L)$ and $y = 1$.

function defined as $u_1 = \partial_y \Psi$, $v_1 = -\partial_x \Psi$, elimination of pressure and representation of the unknowns in the form of Fourier expansions

$$\Psi(x,y) = \sum_{n=-\infty}^{n=+\infty} \Phi^{(n)}(y)\,\mathrm{e}^{\mathrm{i}n\alpha x}, \quad u_1(x,y) = \sum_{n=-\infty}^{n=+\infty} f_u^{(n)}(y)\,\mathrm{e}^{\mathrm{i}n\alpha x}, \quad v_1(x,y) = \sum_{n=-\infty}^{n=+\infty} f_v^{(n)}(y)\,\mathrm{e}^{\mathrm{i}n\alpha x}, \tag{2.4}$$

where $\Phi^{(n)} = \Phi^{(-n)*}$, $f_u^{(n)} = f_u^{(-n)*}$, $f_v^{(n)} = f_v^{(-n)*}$, lead to a system of nonlinear ordinary differential equations for the functions $\Phi^{(n)}$, $n \geqslant 0$, in the form

$$\left[D_n^2 - \mathrm{i}n\alpha Re\left(u_0 D_n - D^2 u_0\right)\right]\Phi^{(n)} - \mathrm{i}\alpha Re \sum_{k=-\infty}^{k=+\infty} \left[kD\Phi^{(n-k)} D_k \Phi^{(k)} - (n-k)\Phi^{(n-k)} D_k D\Phi^{(k)}\right] = 0, \tag{2.5}$$

where $D = \mathrm{d}/\mathrm{d}y$, $D_n = D^2 - n^2\alpha^2$. The boundary conditions at the channel walls are expressed in the form

$$u_0\left(y_{\mathrm{L}}(x)\right) + u_1\left(x, y_{\mathrm{L}}(x)\right) = 0, \qquad v_1\left(x, y_{\mathrm{L}}(x)\right) = 0, \tag{2.6a}$$

$$u_1(x,1) = 0, \qquad v_1(x,1) = 0. \tag{2.6b}$$

The above formulation requires one arbitrary closing condition [26,29]. All results presented in this paper have been obtained with the fixed volume flux condition.

The field equations have been solved using spectral methods based on the Chebyshev expansions. The boundary conditions on the smooth wall have been implemented using a variant of the tau technique [26] while the immersed boundary conditions method has been used to enforce boundary conditions at the corrugated wall [32].

It is useful to discuss topology of the corrugation-modified flow field as it may assist in identifying instability mechanisms associated with the corrugation. The following discussion is focused on the simplest case, i.e., corrugation represented by a single Fourier mode with 4S representing distance between the top and bottom of the corrugation (see Section 4.1 for detailed discussion). Streamlines for the parameters values of interest, i.e., $Re = 5000$, $\alpha = 3.5$, $S = 0.0075$, are displayed in Fig. 2A. A slight asymmetry of the flow between the upstream and downstream sides of the "valley" position occurring due to the nonlinear effects is visible. The flow is expected to separate on the downstream side of the "ridge" for sufficiently deep corrugation. While such separation did not occur for the parameter values considered here, the inflectional velocity profiles did develop especially on the downstream side of the "ridge".

Fig. 2B illustrates distribution of vorticity. The reader may note that corrugation deforms the otherwise flat surfaces of iso-vorticity and appears to act as a source of additional vorticity. This may lead to an interesting flow dynamics by itself as well as to the activation of the so-called CL1 and CL2 mechanisms [33].

The streamline pattern demonstrates the presence of centrifugal forces whose magnitude can be determined by studying distribution of streamline curvature. The curvature K can be evaluated according to the formula

$$K = \left(u_1^2 \frac{\partial v_1}{\partial x} - v_1^2 \frac{\partial u_1}{\partial y} - 2v_1 u_1 \frac{\partial u_1}{\partial x}\right) \Big/ \left(v_1^2 + u_1^2\right)^{3/2} \tag{2.7}$$

and its distribution is illustrated in Fig. 2C for two corrugation periods. The curvature is negative over approximately first half of the period, and positive over the second half. Potential for instability driven by centrifugal effect is expressed in terms of the Rayleigh criterion [34] that states that a necessary and sufficient condition for stability is that square of circulation should not decrease anywhere. This criterion had been derived in the case of flow between circular cylinders using a polar system of coordinates where the positive direction is uniquely defined. In the present case the flow is described in terms of a Cartesian system and thus the positive direction corresponds to increasing y in the area where the curvature is negative, and decreasing y in the area where the curvature is positive. The local circulation Γ can be evaluated according to the formula

$$\Gamma = \left(|\bar{v}|/K\right) = \left(v_1^2 + u_1^2\right)^2 \Big/ \left(u_1^2 \frac{\partial v_1}{\partial x} - v_1^2 \frac{\partial u_1}{\partial y} - 2v_1 u_1 \frac{\partial u_1}{\partial x}\right) \tag{2.8}$$

and its distribution is illustrated in Fig. 2D. Shaded area denotes the flow sectors where the Rayleigh criterion is violated.

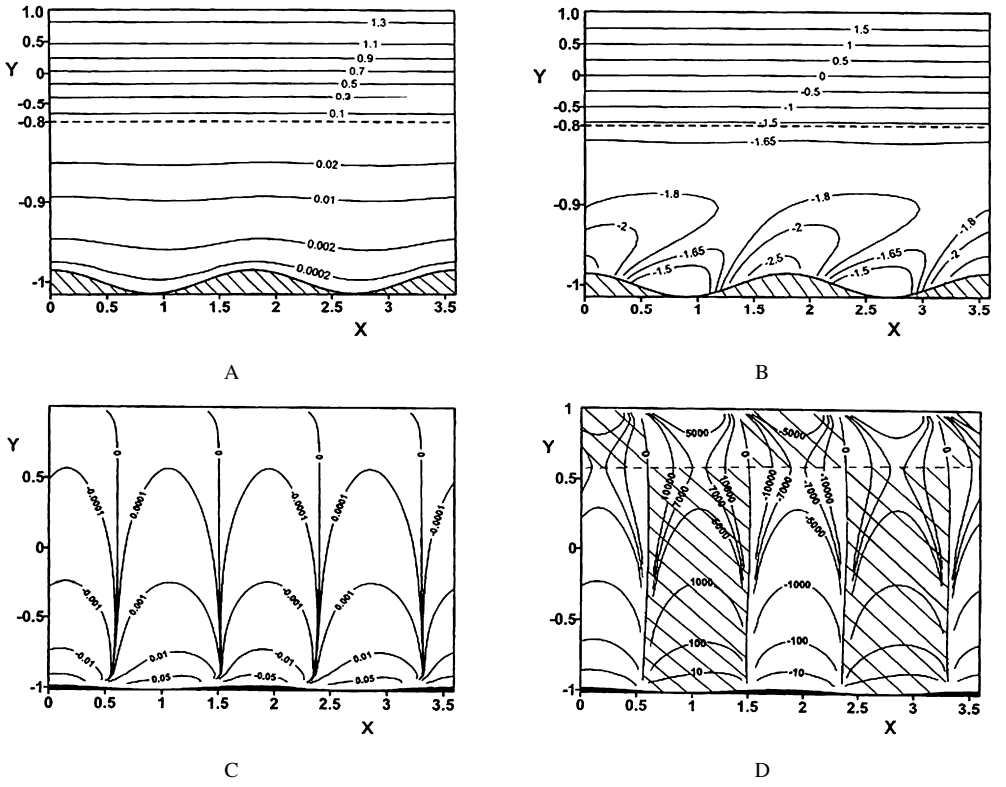

Fig. 2. Properties of the flow for Reynolds number $Re = 5000$, the corrugation wave number $\alpha = 3.5$ and the corrugation amplitude $S = 0.0075$. A – streamlines, B – vorticity, C – streamline curvature, D – circulation. Shaded area denotes sector in the flow field where the Rayleigh criterion is violated.

3. Stability analysis

The linear stability characteristics of the flow in a channel with smooth walls are well known. In this section we shall inquire how these characteristics change owing to the presence of wall corrugation.

Detailed description of the problem formulation can be found in [26,29]. The following presentation is limited to a short outline. We begin with the governing equations in the form of vorticity transport and continuity equations. Unsteady, three-dimensional disturbances are superimposed on the mean part in the form

$$\boldsymbol{\omega} = \boldsymbol{\omega}_2(x, y) + \boldsymbol{\omega}_3(x, y, z, t), \qquad \mathbf{V} = \mathbf{V}_2(x, y) + \mathbf{V}_3(x, y, z, t), \tag{3.1}$$

where subscripts 2 and 3 refer to the mean flow and the disturbance field, respectively. Eq. (3.1) is substituted into the field equations, the mean part is subtracted and the equations are linearized. The resulting disturbance equations have the form

$$\frac{\partial \boldsymbol{\omega}_3}{\partial t} + (\mathbf{V}_2 \cdot \nabla)\boldsymbol{\omega}_3 - (\boldsymbol{\omega}_3 \cdot \nabla)\mathbf{V}_2 + (\mathbf{V}_3 \cdot \nabla)\boldsymbol{\omega}_2 - (\boldsymbol{\omega}_2 \cdot \nabla)\mathbf{V}_3 = Re^{-1}\nabla^2\boldsymbol{\omega}_3, \tag{3.2a}$$

$$\nabla \cdot \mathbf{V}_3 = 0, \qquad \boldsymbol{\omega}_3 = \nabla \times \mathbf{V}_3 \tag{3.2b,c}$$

and are subject to the homogeneous boundary conditions

$$\mathbf{V}_3(x, 1, z) = 0, \qquad \mathbf{V}_3(x, y_L(x), z) = 0, \tag{3.2d}$$

where y_L is given by Eq. (2.2). These boundary conditions are, in general, incomplete [27] and require an additional closing condition. All results presented in this paper have been obtained with the constant-mass-flux constraint.

Our interest is in the asymptotic stability and thus the t and z dependence can be separated in the usual manner leading to the solution in the form

$$\mathbf{v}_3(x, y, z, t) = \big[u_3(x, y), v_3(x, y), w_3(x, y)\big]\, \mathrm{e}^{\mathrm{i}(\delta x + \beta z - \sigma t)} + CC, \tag{3.3}$$

where δ and β are real and account for the streamwise and spanwise periodicity of the disturbance field, respectively. The exponent σ is complex and its imaginary and real parts describe the rate of growth and the frequency of the disturbances, respectively, and the function $[u_3, v_3, w_3]$ describes the amplitude of the disturbance velocity vector. The disturbance amplitude is modulated by the surface corrugation leading to the final form of the disturbance velocity vector

$$\mathbf{v}_3(x,y,z,t) = \sum_{m=-\infty}^{m=+\infty} \left[g_u^{(m)}(y), g_v^{(m)}(y), g_w^{(m)}(y)\right] \mathrm{e}^{\mathrm{i}[(\delta+m\alpha)x+\beta z-\sigma t]} + CC \tag{3.4}$$

and, eventually, to the eigenvalue problem for (δ, β, σ) for the ordinary differential equations describing functions $g_u^{(m)}, g_v^{(m)}, g_w^{(m)}$. The system of equations governing $g_u^{(m)}, g_v^{(m)}, g_w^{(m)}$ has the form

$$S^{(m)}\left(t_m g_w^{(m)} - \beta g_u^{(m)}\right) + C g_v^{(m)} = \mathrm{i}Re \sum_{n=-\infty}^{n=\infty} \left(W_u^{(m,n)} g_u^{(m-n)} + W_v^{(m,n)} g_v^{(m-n)} + W_w^{(m,n)} g_w^{(m-n)}\right), \tag{3.5a}$$

$$T^{(m)} g_v^{(m)} = -Re \sum_{n=-\infty}^{n=\infty} \left(B_u^{(m,n)} g_u^{(m-n)} + B_v^{(m,n)} g_v^{(m-n)} + B_w^{(m,n)} g_w^{(m-n)}\right), \tag{3.5b}$$

$$\mathrm{i}t_m g_u^{(m)} + D g_v^{(m)} + \mathrm{i}\beta g_w^{(m)} = 0, \quad -\infty < m < \infty, \tag{3.5c}$$

where the explicit forms of the operators T, S, C, W, B are given in Appendix A and $t_m = m\alpha + \delta$. Operators S, C and T are referred to as the Squire [35], coupling and Orr–Sommerfeld operators [36,37], respectively, owing to their analogy with the similar operators in the smooth-wall case [26].

The boundary conditions for the individual modes have the form

$$g_u^{(m)}(1) = g_v^{(m)}(1) = g_w^{(m)}(1) = g_u^{(m)}(y_\mathrm{L}) = g_v^{(m)}(y_\mathrm{L}) = g_w^{(m)}(y_\mathrm{L}) = 0, \quad -\infty < m < +\infty. \tag{3.6}$$

Eqs. (3.5) with boundary conditions (3.6) have nontrivial solutions only for certain combinations of parameters δ, σ and β. The required dispersion relation has to be determined numerically. For the purposes of calculations, the problem is posed as an eigenvalue problem for σ. Eqs. (3.5) are discretized with spectral accuracy using Chebyshev expansions. Boundary conditions at the upper wall are implemented using a version of the tau technique [26] while boundary conditions at the rough lower wall are implemented using the concept of immersed boundary conditions [29].

4. Discussion of results

The present analysis is relevant to the low-disturbance environment and all results have been obtained with the fixed-mass-constraint. The plane Poiseuille flow (i.e. flow in a channel with smooth walls) becomes linearly unstable at $Re = 5772.22$ and the critical disturbance has the form of a two-dimensional wave traveling in the streamwise direction. Such waves are typically referred to as the Tollmien–Schlichting (TS) waves. Questions to be answered in this analysis are (i) how the presence of wall corrugation affects the traveling-wave (TS) instability and (ii) whether the corrugation can induce any new instability. The flow response does, in general, depend on the corrugation shape. We work with the spectral model of corrugation geometry and thus the simplest possible corrugation form is that represented by a single Fourier mode, i.e., wavy-wall model. We begin with a detailed discussion of this model and then proceed to analyze more complex geometries. Three classes of shapes have been chosen with the reason for their selection explained in Section 5. The analysis is focused on the asymptotic instability and the issues related to transient growth are not addressed. The reader may recall that α denotes the wave number of the corrugation, and δ and β denote the streamwise and spanwise disturbance wave numbers, respectively.

4.1. Wavy-wall model

The shape of the lower wall is represented by Eq. (2.2) where $S^{(1)} = S^{(-1)} = S$ are real and $S^{(n)} = 0$ for $n \neq \pm 1$. The shape of the wall is completely parameterized by the corrugation amplitude S and the corrugation wave number α.

4.1.1. Vortex instability

The presence of corrugation gives rise to instability that results in the amplification of disturbances in the form of streamwise vortices. These vortices are fixed with respect to the wall, i.e., $\mathrm{Real}(\sigma) = 0$, are modulated in the streamwise direction by the corrugation itself (i.e., $\alpha = \delta$) and are qualitatively similar to those studied in the case of Couette flow [29]. The complete spectrum of the complex amplification σ corresponding to the flow Reynolds number $Re = 5000$, the corrugation wave number $\alpha = 2$, the corrugation amplitude $S = 0.0075$ and the vortex wave number $\beta = 2$ is shown in Fig. 3. This spectrum has been re-computed a number of times using different number of Chebyshev polynomials and Fourier modes and only values that did not depend on the numerical parameters were plotted. The same figure displays Orr–Sommerfeld and Squire spectra for the flat wall for $\alpha = 0, 2, 4$ and $\beta = 2$. The reader may note that the complete spectrum consists of a union of (interdependent) spectra associated with individual Fourier modes. These spectra have characteristic A, P and S branches (according to the nomenclature introduced in [38]) and decouple in the limit $S \to 0$. It can be seen that all modes are stable in the absence of corrugation, as shown in Fig. 4 displaying top of the spectrum. Introduction of the corrugation couples all these modes and destabilizes the mode with $\mathrm{Real}(\sigma) = 0$. The two least stable modes connect to the symmetric and anti-symmetric Squires modes for $S \to 0$ [29] with Fig. 5 illustrating the evolution of the least stable modes as a function of S. The distinct limit $S = 0$ can be determined analytically, i.e., $\sigma = -\mathrm{i}(\beta^2 + \pi^2/4)/Re$. It is worth pointing out that the general structure of the spectrum is not affected by the corrugation; it is the interaction between various modes that results in the promotion of one eigenvalue into the unstable half-plane.

Instability leading to the formation of streamwise vortices has been identified in the case of convergent-divergent channels [30]. Two modes of instability (symmetric and anti-symmetric) have been found in that case, while only one exists in the present case in the range of parameters studied, most likely because of the geometric asymmetry of the channel.

The disturbance velocity field corresponding to the unstable eigenvalue is illustrated in Fig. 6. The x-velocity component is much bigger than the remaining two, which is a characteristic feature of streamwise vortices in shear layers. The actual topology of the disturbance velocity field may be quite complex as backflow in the x-direction is possible as illustrated in Fig. 7. This topology is illustrated for $Re = 5000$, $\alpha = \beta = 2$, $S = 0.0075$ in Fig. 8 which displays spanwise cuts through the velocity field starting at $x = 0$ every $\lambda/8$, where $\lambda = 2\pi/\alpha$ denotes the length of the period. The flow field consists of two layers of vortex pairs rotating in the opposite sense above the corrugation peak (Fig. 8A), with the top layer occupying most of the available space. The bottom vortex partially disappears

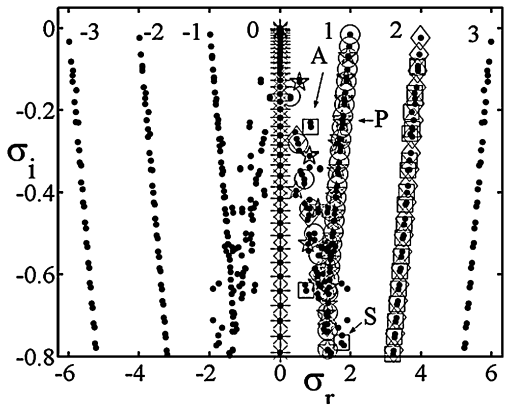

Fig. 3. Spectra for the flow Reynolds number $Re = 5000$, the corrugation wave number $\alpha = 2$ and amplitude $S = 0.0075$, and the vortex wave number $\beta = 2$. Black circles show full spectrum, crosses and X's show the Orr–Sommerfeld and Squire spectra for $\alpha = 0$, $\beta = 2$, respectively, stars and circles show the Orr–Sommerfeld and Squire spectra for $\alpha = 2$, $\beta = 2$, respectively, and squares and diamonds show the Orr–Sommerfeld and Squire spectra for $\alpha = 4$, $\beta = 2$, respectively. A, P and S branches of the spectrum for the first Fourier mode are denoted using symbols A, P and S, respectively. The numbers shown correspond to the index "m" in Eq. (3.5) identifying Fourier modes.

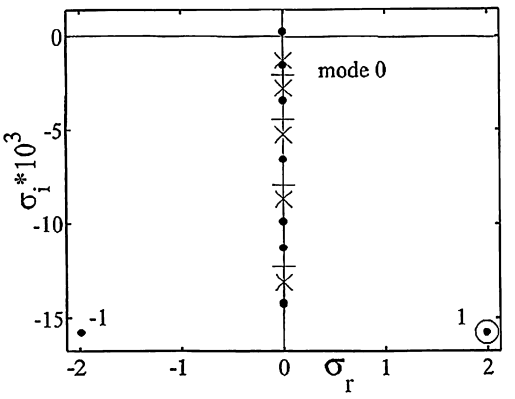

Fig. 4. Top of the spectrum shown in Fig. 3. Notation is the same as in Fig. 3.

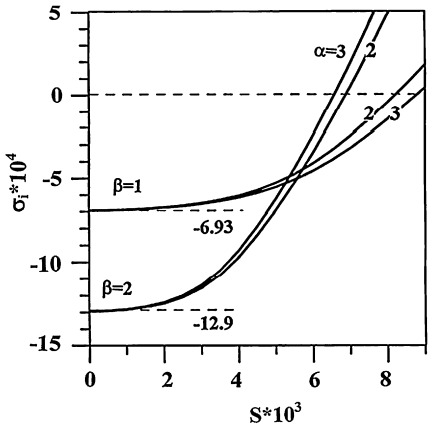

Fig. 5. Amplification rate Imag(σ) of the vortex-like disturbances with the spanwise wave numbers $\beta = 1$ and $\beta = 2$ induced by the wavy-wall with the wave numbers $\alpha = 2$ and $\alpha = 3$ for $Re = 5000$ as a function of the corrugation amplitude S.

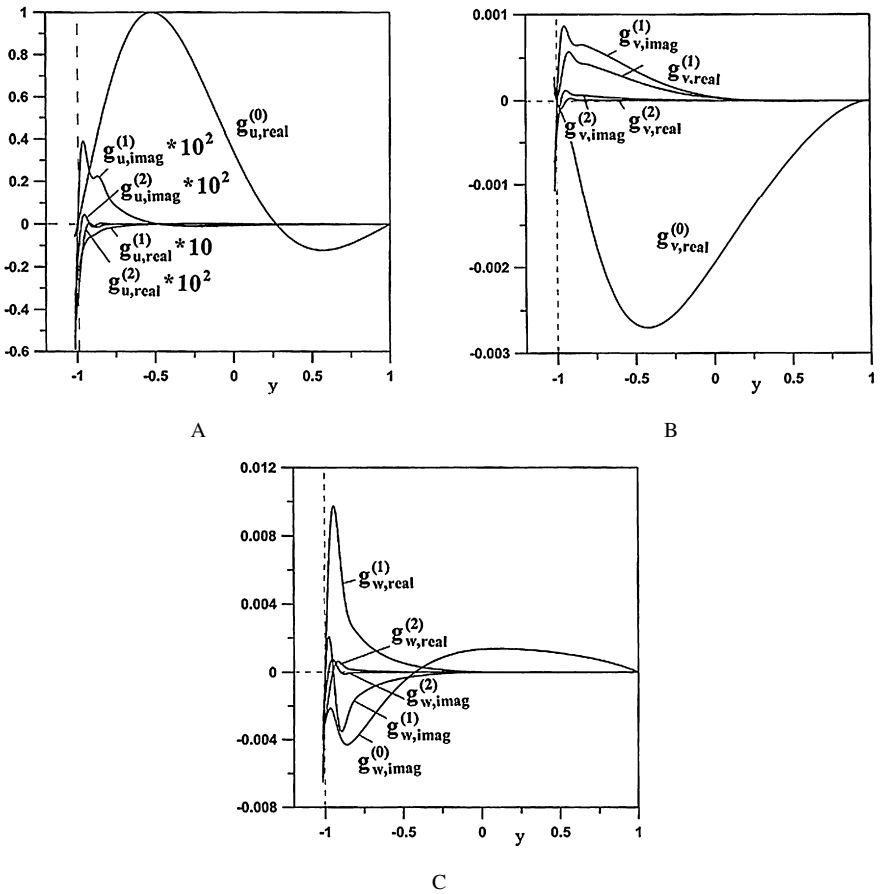

Fig. 6. Eigenfunctions $g_u^{(m)}$, $g_v^{(m)}$, $g_w^{(m)}$, $m = 0, 1, 2$, associated with the vortex-like disturbances with the wave number $\beta = 2$ induced by the wavy-wall with the wave number $\alpha = 2$ and the amplitude $S = 0.0075$ for the flow Reynolds number $Re = 5000$ and normalized with condition $\max(g_u^{(0)}) = 1$. Figs. 6A, 6B, 6C display functions $g_u^{(m)}$, $g_v^{(m)}$, $g_w^{(m)}$, respectively.

and changes direction of motion with a saddle point forming between both layers at $x = \lambda/8$ (Fig. 8B). Here we use the nomenclature of critical-point theory [39]. The vortex structure completely disappears at $x = \lambda/4$ (Fig. 8C) and $x = 3\lambda/8$ (Fig. 8D) with fluid moving from left to right on the left side of the figure. The double-vortex layer

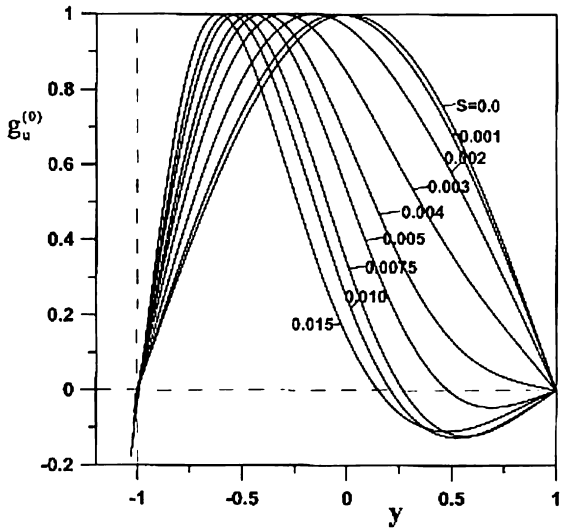

Fig. 7. Evolution of the eigenfunction $g_u^{(0)}$ associated with the vortex-like disturbances as a function of the wavy-wall amplitude S for the corrugation wave number $\alpha = 2$, the vortex wave number $\beta = 2$ and the flow Reynolds number $Re = 5000$. Normalization condition $\max(g_u^{(0)}) = 1$.

re-emerges at $x = \lambda/2$ (Fig. 8E) but with the lower vortex rotating in the same sense as the upper one and a saddle point forming between them. This location corresponds to the bottom of the corrugation. The lower vortex partially disappears at $x = 5\lambda/8$ while maintaining a direction of motion consistent with the upper vortex and without forming any critical points (Fig. 8F). The same but more pronounced structure exists at $x = 6\lambda/8$ and $x = 7\lambda/8$ (Figs. 8F–H). In summary, two vortex layers can be clearly identified but only above corrugation extremes. There is a rapid flow re-adjustment downstream from the corrugation peak with the qualitatively similar structure persisting until the flow approaches the bottom of the corrugation where another rapid re-adjustment takes place and a new structure re-emerges and persists until the flow again reaches corrugation peak. The re-adjustment zones are characterized by a double-vortex layer, but with the lower vortex rotating in a different sense above the corrugation peak and the corrugation bottom.

The differences between the flow in the zones downstream and upstream from the corrugation peak are also illustrated in Fig. 9, which displays a modified disturbance velocity field in the (x, y) plane at $z = 0$. The modification involves elimination of the zero mode $g_u^{(0)}$ from the u velocity component; this mode is an order of magnitude larger than the remaining modes (see Fig. 6) and thus conceals a streamwise modulation of the velocity field. The flow modulation has a simple form. As the flow approaches the corrugation peak, it is forced to change direction owing to the blocking effect of the corrugation; the resulting instability drives the flow in the spanwise direction resulting in the formation of an unstable node (source) close to the corrugated wall. The corresponding sink (stable node) is located next to the smooth wall but in the diverging section of the channel. The critical points at the corrugated wall just downstream from the corrugation peak and at the smooth wall just upstream from the corrugation peak can be interpreted as symmetric saddles where streamlines separating the streams flowing between different pairs of sources and sinks terminate.

The streamwise evolution of the vortex structure suggests that the vortices may be driven by the centrifugal force [29]. The reader may recall that the centrifugal instability may occur over concave as well as convex walls [40]. The area where the corrugation height increases corresponds to the converging-flow section where the Rayleigh criterion suggests the existence of a centrifugal mechanism (Fig. 2). As the fluid moves through the stable and unstable zones, the vortices are formed in the converging section and are attenuated in the diverging section. The question whether the whole vortex system grows or decays in time hinges on the delicate balance between the instability-driving centrifugal force in the converging section and the instability-damping centrifugal force in the diverging section and the stabilizing effect of viscous dissipation in the whole channel. Results of this analysis show that it is possible to find a combination of the flow conditions and the corrugation amplitude where the vortex system does indeed grow in time.

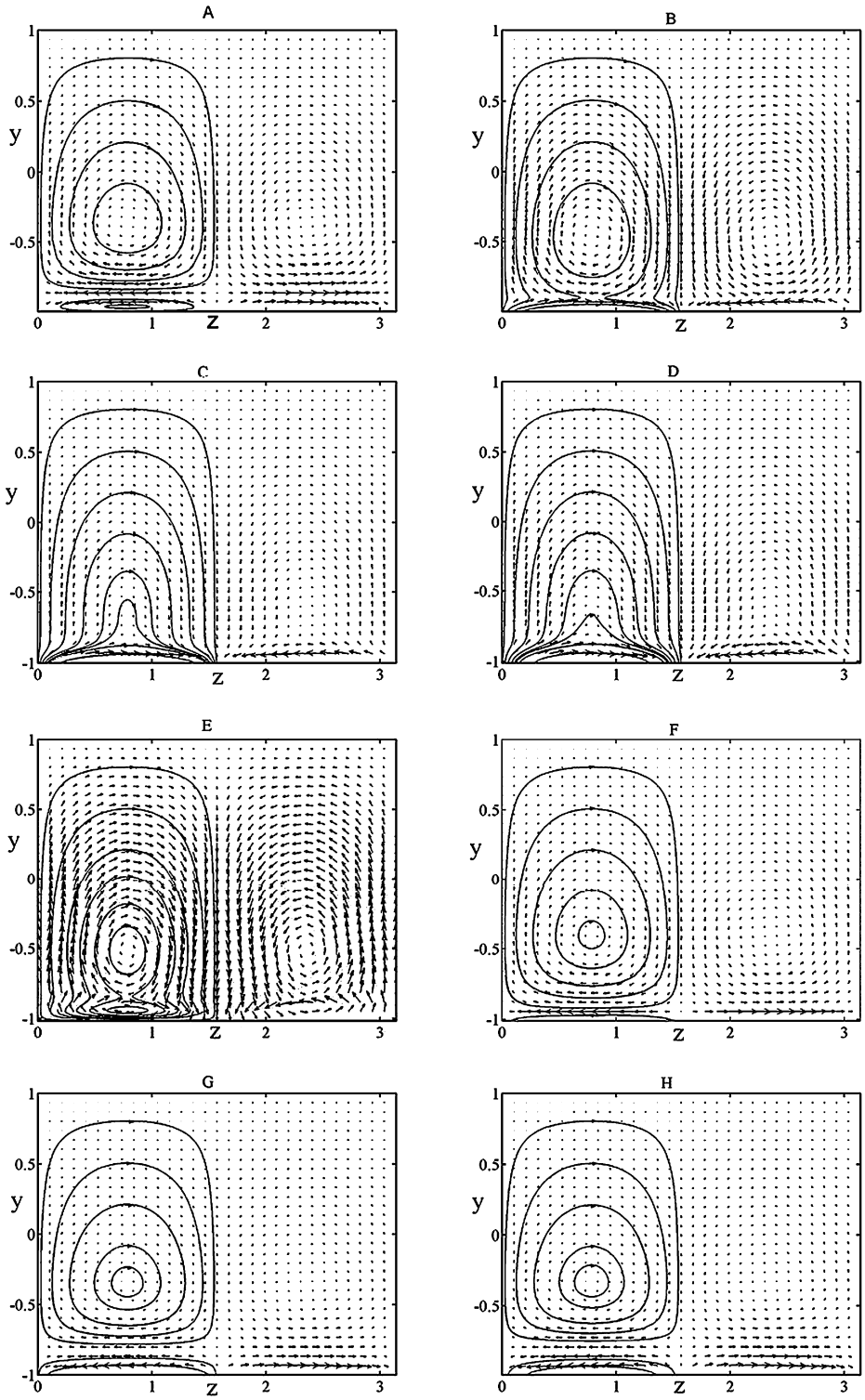

Fig. 8. Distribution of the (y, z) component of the disturbance velocity vector associated with the vortex-like disturbances for $z \in (0, 2\pi/\beta)$, the vortex wave number $\beta = 2$, the wavy-wall wave number $\alpha = 2$, the flow Reynolds number $Re = 5000$ and the corrugation amplitude $S = 0.0075$. The disturbance velocity vector is normalized with condition $\max(g_u^{(0)}) = 1$. Figs. 8A–8H correspond to $x = 0, \lambda/8, \lambda/4, 3\lambda/8, \lambda/2, 5\lambda/8, 3\lambda/4, 7\lambda/8$, respectively, where $\lambda = 2\pi/\alpha$ denotes one wavelength of the corrugation. Continuous lines illustrate trajectories in the phase plane.

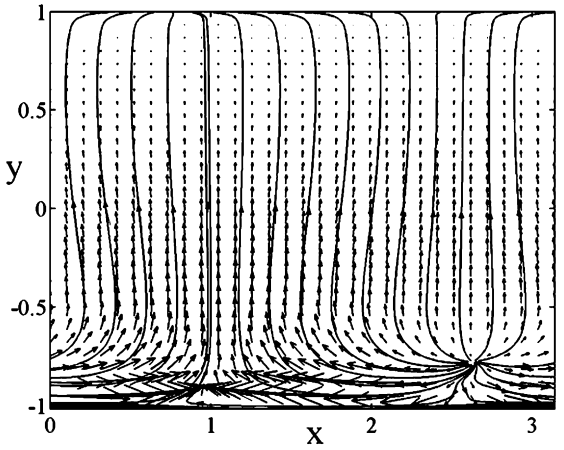

Fig. 9. Distribution of the (x, y) component of the modified disturbance velocity vector associated with the vortex-like disturbances for $x \in (0, 2\pi/\alpha)$ at $z = 0$. The remaining conditions are the same as in Fig. 8. The modification involves elimination of the zero-th mode from the u-velocity component, i.e., elimination of $g_u^{(0)}$.

While the above discussion points to the centrifugal origin of the vortices, the reader should keep in mind the existence of two other possible mechanisms proposed in the context of Langmuir circulation and commonly refereed to as the CL1 and CL2 mechanisms [29,33,41,42]. While the disturbances have no streamwise vorticity when $S = 0$ [29], such vorticity is created by "bending" of the plane vortex sheets by surface corrugation which may lead to interesting dynamics that has been studied most closely in the context of the CL1 mechanism. It is not possible to rule out any of the above mechanisms as all of them may lead to the formation of streamwise vortices, while the indirect evidence in the form of streamwise evolution of the flow-field structure points towards the centrifugal effect.

The unstable eigenvalue has been traced through the parameter space in order to determine physical characteristics of the instability. The amplification rates $\mathrm{Imag}(\sigma)$ are illustrated in Fig. 10 for the flow Reynolds number $Re = 5000$ and the corrugation amplitude $S = 0.0075$. The range of the "active" corrugation wave numbers extends from $\alpha \approx 1.4$ to $\alpha \approx 7$ where the term "active" refers to the wave numbers that give rise to the instability. Each "active" corrugation wave number gives rise to a band of vortices whose wavelength is bounded from above and below. The amplified-vortex wave numbers are always contained in the interval $\sim 1.2 < \beta < \sim 3.7$ but the vortices that are actually amplified are contained in a smaller subinterval whose length and location change as a function of the corrugation wave number.

Fig. 11 displays the neutral surface in the (α, β, S) space for $Re = 5000$. The interior of this surface corresponds to the flow conditions giving rise to the instability. The shape of the neutral surface shows that the range of the "active" corrugation wave numbers α as well as the range of the resulting unstable vortex wave numbers β increase rapidly with an increase of the corrugation amplitude S. Similar results obtained for $Re = 10^4$ and displayed in Fig. 12 demonstrate that this increase is more rapid for higher values of Re, where it results in much wider ranges of "active" α's and resulting β's. It can also be seen that the instability occurs at much smaller corrugation amplitudes when Re is higher.

Fig. 13 displays the neutral surface in the (α, β, Re) space for $S = 0.007$. A rapid increase of the range of "active" corrugation wave numbers α and the resulting vortex wave numbers β as Re increases is clearly visible.

One of the objectives of this analysis is the determination of the critical conditions for this instability. A cut corresponding to a particular wave number $\alpha = \text{const}$ through the neutral surface shown in Fig. 13 defines the critical Reynolds number for this particular α and $S = 0.007$. A similar cut through the neutral surface shown in Fig. 11 determines the amplitude S for which $Re = 5000$ represents the critical value. It is convenient for presentation of the results to introduce a global critical Reynolds number $Re_{g,\mathrm{cr}}$ that defines the critical conditions for the onset of the instability for a given corrugation amplitude S regardless of its wavelength. Such global critical conditions, which include the critical corrugation wave number $\alpha_{g,\mathrm{cr}}$ and the critical vortex wave number $\beta_{g,\mathrm{cr}}$, correspond to the tip of the neutral surface shown in Fig. 13. Variations of the global critical conditions as a function of the corrugation amplitude S are illustrated in Fig. 14. It can be seen that the most effective in terms of flow-destabilization corrugation

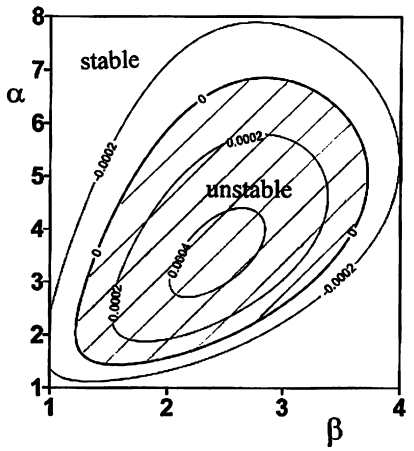

Fig. 10. Amplification rates Imag(σ) of disturbances in the form of streamwise vortices as a function of the corrugation wave number α and the vortex wave number β for the flow Reynolds number $Re = 5000$ and the wavy-wall of amplitude $S = 0.0075$.

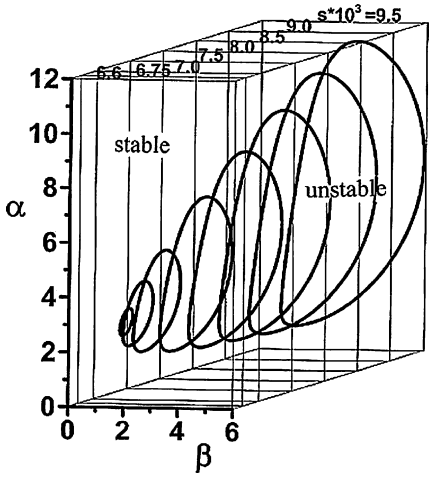

Fig. 11. The neutral surface describing instability giving rise to the vortex-like disturbances for the flow Reynolds number $Re = 5000$ as a function of the corrugation amplitude S, the corrugation wave number α and the vortex wave number β for the wavy-wall corrugation model.

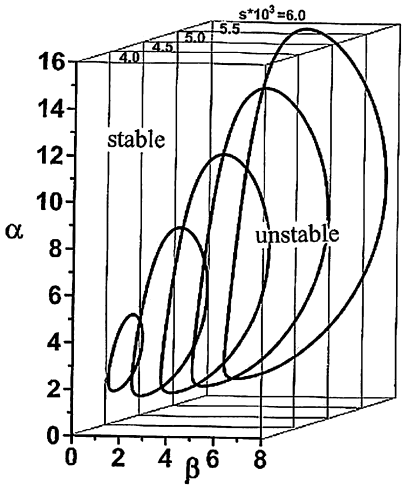

Fig. 12. The same as in Fig. 11 but with the Reynolds number $Re = 10^4$.

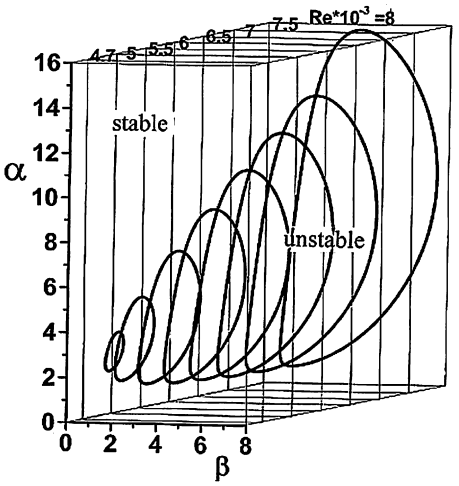

Fig. 13. The neutral surface describing instability giving rise to the vortex-like disturbances for the corrugation amplitude $S = 0.007$ as a function of the flow Reynolds number Re, the corrugation wave number α and the vortex wave number β for the wavy-wall corrugation model.

wave number is $\alpha \approx 3$ while the vortex wave number most likely to emerge from the instability is $\beta \approx 2$. The values of $Re_{g,\mathrm{cr}}$ can be expressed for small values of S using simple correlation in the form

$$\ln(Re_{g,\mathrm{cr}}) = -1.3205 \ln(S) + 1.8888 \tag{4.1}$$

which provides accuracy no worse then 1% when $S < 0.01$. This correlation is displayed in Fig. 14.

The area below the critical curve defines the flow conditions when the corrugation does not destabilize the vortex-like disturbances and is in this sense hydraulically inactive, regardless of its wave number. The area above this curve defines flow conditions where there exists at least one "active" corrugation wave number. The reader should note that the flow does not automatically become unstable for $Re > Re_{g,\mathrm{cr}}$; the instability occurs if and only if the particular corrugated wall contains an "active" corrugation wave number. The reader should also note that changes in the corrugation geometry for $Re > Re_{g,\mathrm{cr}}$ may either stabilize or destabilize the system. The neutral surface in the hyperspace

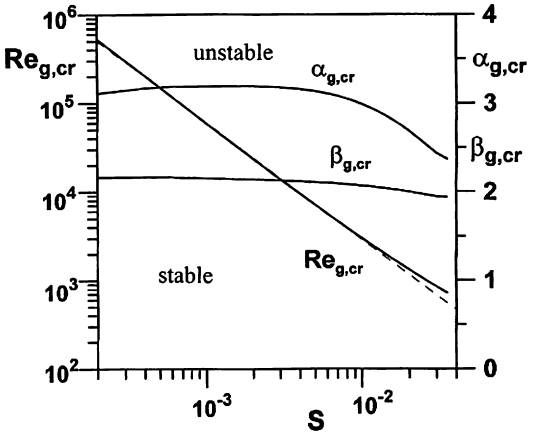

Fig. 14. Variations of the global critical stability conditions, i.e., $Re_{g,\mathrm{cr}}$, $\alpha_{g,\mathrm{cr}}$ and $\beta_{g,\mathrm{cr}}$, for disturbances in the form of streamwise vortices induced by the wavy-wall corrugation. Thin dash line corresponds to the correlation (4.1).

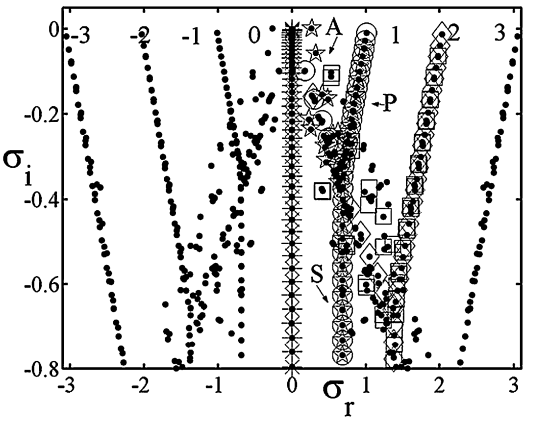

Fig. 15. Spectra for the flow Reynolds number $Re = 6000$, the corrugation wave number $\alpha = 1.02$ and the disturbance wave numbers $\delta = 1.02$ and $\beta = 0$. Black circles show full spectrum, crosses and X's show the Orr–Sommerfeld and Squire spectra for $\delta = 0$, $\beta = 0$, respectively, stars and circles show the Orr–Sommerfeld and Squire spectra for $\delta = 1.02$, $\beta = 0$, respectively, and squares and diamonds show the Orr–Sommerfeld and Squire spectra for $\delta = 2.04$, $\beta = 0$, respectively. A, P and S branches of the spectrum for the first Fourier mode are denoted using symbols A, P and S, respectively. The numbers shown correspond to the index "m" in Eq. (3.3) identifying Fourier modes.

formed by Re, α, β and S may have many local maxima and changes of α and S can move the system between these maxima. Such system characteristics had been observed in the present study, but have not been explored in details; there is also experimental evidence to this effect [43]. Results given in this paper identify the absolute or global "maximum" that guarantees that no instability occurs for $Re < Re_{g,\mathrm{cr}}$ regardless of the corrugation geometry.

It is useful to comment on the expected evolution of the flow assuming that the corrugation is able to induce vortex-type instability. One route of inquiry is the nonlinear evolution of the vortices; it is not known at present whether weak nonlinear effects enhance or suppress the instability. The second route is associated with the fact that the presence of the vortices leads to a significant re-arrangement and rapid three-dimensionalization of the flow. Uplifting of low-momentum fluid away from the wall leads to the formation of streaks with highly distorted streamwise and spanwise velocity profiles that are subject to very strong secondary instabilities. The experimental evidence available in the case of Görtler instability [19] suggests that the flow is likely to follow the latter route and indeed, the secondary instabilities are expected to have the form similar to that found in the case of Görtler vortices. Additional complications may arise owing to the presence of strong shear layers formed by the instability at the corrugated wall, especially in the re-adjustment zones above corrugation peak and corrugation bottom. These layers may induce secondary instabilities not associated with those driven by the central vortices. The above discussion suggests that the flow evolution past the critical conditions is likely to require fully nonlinear analysis, with weakly nonlinear models likely to be unable to capture its salient features, similar to the case of diverging-converging channels [30].

4.1.2. Traveling-wave instability

Two-dimensional traveling-wave instability has been studied both theoretically [27,44] and experimentally [28]. The present analysis is focused on the three-dimensional aspects of this instability. While it is known that two-dimensional waves play the role of critical disturbances in smooth channels [35], it remains to ascertain whether they remain critical in the case of a corrugated channel.

We begin discussion with the description of the spectrum of the complex amplification σ for a typical corrugation geometry, flow conditions and disturbance wave numbers, i.e.,

$$Re = 6000, \quad S = 0.0085, \quad \alpha = 1.02, \quad \beta = 0, \quad \delta = 1.02,$$

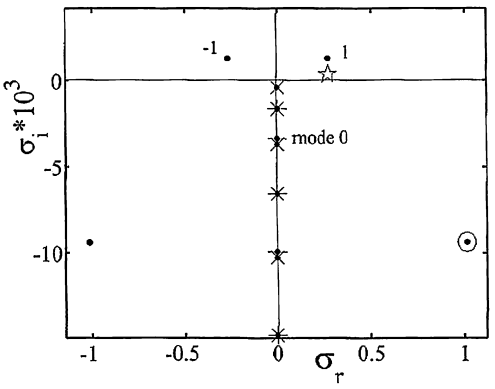

Fig. 16. Top of the spectrum shown in Fig. 15. Notation is the same as in Fig. 15.

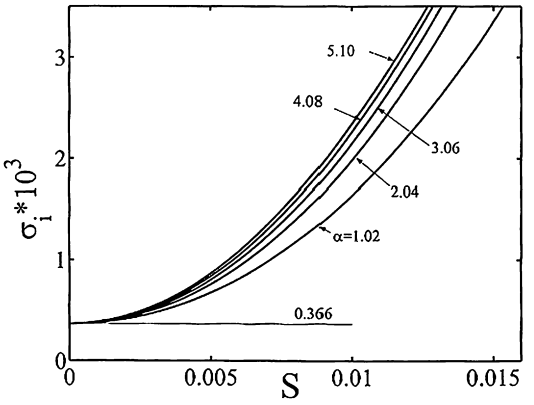

Fig. 17. Amplification rate Imag(σ) of two-dimensional traveling wave with the wave number $\delta = 1.02$ in the flow with $Re = 6000$ in channels with the wavy-wall corrugation characterized by the wave numbers $\alpha = 1.02, 2.04, 3.06, 4.08, 5.10$ as a function of the corrugation amplitude S.

which is shown in Fig. 15. This spectrum has been computed in the same manner as spectrum for the vortices discussed previously. The same figure displays Orr–Sommerfeld and Squire spectra for the smooth channel for $\delta = 0, 1.02, 2.04$ and $\beta = 0$. The complete spectrum consists of a union of spectra associated with different Fourier modes with A, P and S branches clearly visible. The unstable mode, the so-called Tollmien–Schlichting (TS) wave [45,46] is well visible in Fig. 16 displaying the top of the spectrum. Introduction of corrugation couples all modes and increases the amplification of the TS wave (see Fig. 16). The increase of the amplification and connection between the TS waves in the smooth channel and traveling waves in a corrugated channel is illustrated in Fig. 17 displaying variations of the amplification as a function of the corrugation amplitude S for the disturbance wave numbers $\delta = 1.02$, $\beta = 0$. The general structure of the spectrum is not affected by the corrugation; it is the interaction between various Fourier modes that results in the destabilization of the TS wave.

The critical-stability conditions for the two-dimensional waves have been given in [27]. The properties of oblique waves are illustrated in Fig. 18 which displays the neutral-stability curves determined for the fixed values of the flow Reynolds number Re and the corrugation amplitude S but for different fixed values of the wave obliqueness, i.e., $\beta/\delta =$ const. The results shown are for three combinations of Re and S, i.e., (i) $Re = 5000$ and $S = 0.009$, (ii) $Re = 6000$ and $S = 0.001$, and (iii) $Re = 6000$ and $S = 0.0085$; the first case is nominally subcritical while the last two are nominally supercritical. It can be seen (Fig. 18) that the increase of the obliqueness of the disturbance reduces the ranges of the "active" corrugation wave numbers α and the unstable disturbance wave numbers δ. Variation of the disturbance maximum amplification as a function of the disturbance obliqueness illustrated in Fig. 19A demonstrates that the two-dimensional waves determine the critical stability conditions. The phase speed of the most amplified disturbances changes little as a function of the wave obliqueness, as illustrated in Fig. 19A. The most amplified streamwise wave number also does not change very much as a function of the wave obliqueness, as shown in Fig. 19B, while the corrugation wave number corresponding to the most amplified disturbance can change significantly depending on the flow conditions (Fig. 19B). All these results demonstrate that in the range of parameters of interest in this analysis the two-dimensional waves determine the critical stability conditions. The variations of the relevant global critical conditions, i.e., $Re_{g,\mathrm{cr}}$, $\alpha_{g,\mathrm{cr}}$ and $\beta_{g,\mathrm{cr}}$ as a function of the corrugation amplitude S, have been given in [27]. The most effective, as far as flow destabilization is concerned, corrugation wave number changes from $\alpha \approx 15$ for $S = 0.006$ to $\alpha \approx 30$ for $S = 0.001$, while the disturbance wave number changes marginally from $\delta \approx 1.02$ in the smooth-wall case to $\delta \approx 1.04$ for $S = 0.006$.

The problem discussed above has been posed as a temporal instability where δ is real and σ is complex whereas the spatial instability with δ complex and σ real is better suited for comparisons with experiments. Formulation of the spatial stability problem is identical to that given in Section 3 with δ being complex and σ real. It is known that in the case of smooth channels spatial amplification can be obtained from the temporal amplification using the Gaster

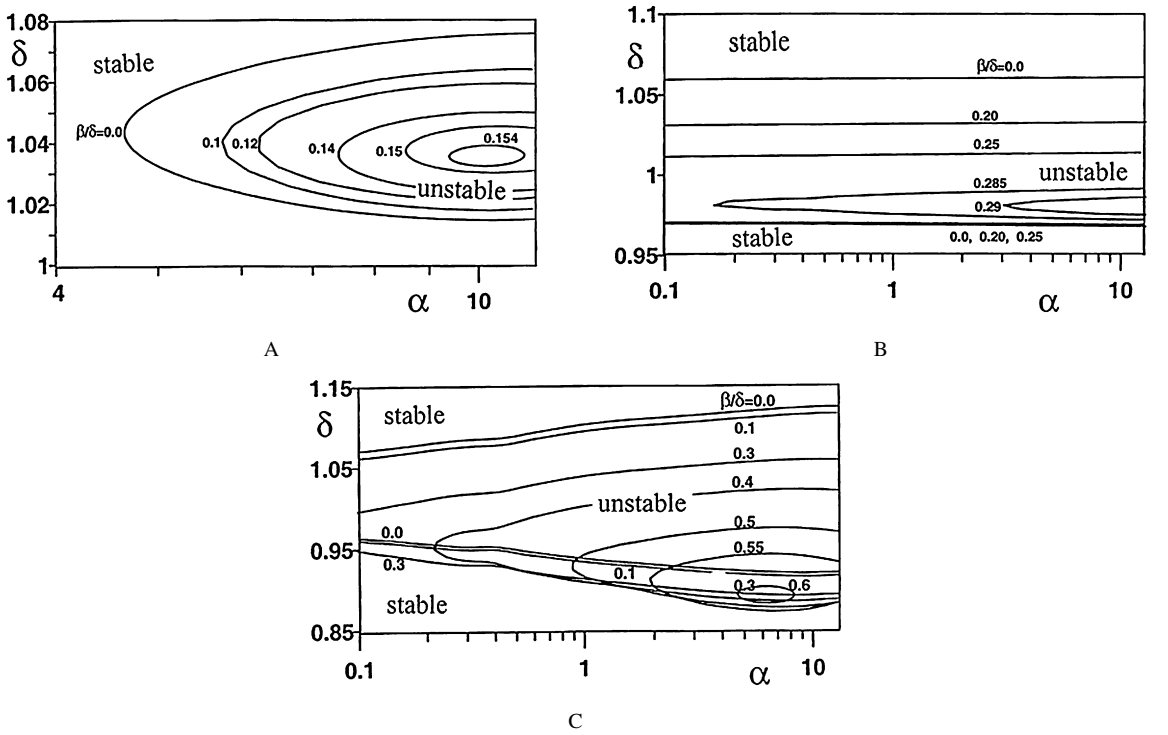

Fig. 18. The neutral stability curves for disturbance in the form of three-dimensional traveling waves as a function of the corrugation wave number α and the streamwise disturbance wave number δ for the wavy-wall corrugation. Each curve corresponds to a different ratio of the spanwise and streamwise disturbance wave numbers β/δ. A – $Re = 5000$, $S = 0.009$; B – $Re = 6000$, $S = 0.001$; C – $Re = 6000$, $S = 0.0085$.

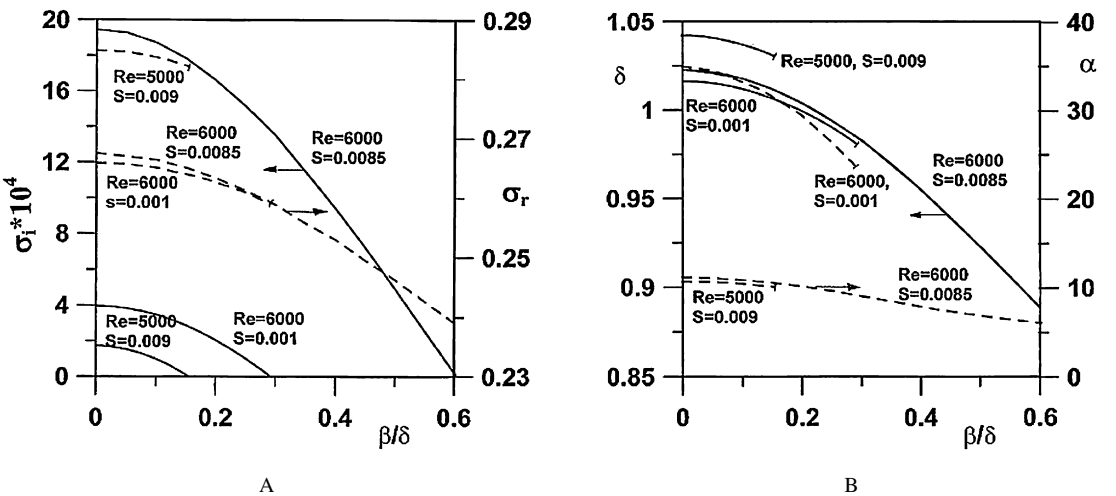

Fig. 19. Variations of the maximum amplification Imag(σ) of the three-dimensional traveling waves as a function of their obliqueness β/δ (Fig. 19A) for the wavy-wall corrugation. The corresponding frequency Real(σ) is shown in the same figure, while the corresponding disturbance streamwise wave number δ and the corrugation wave number α are shown in Fig. 19B for three sets of the flow Reynolds numbers Re and the corrugation amplitudes S. The curves are terminated at the wave obliqueness where the disturbances become stable.

transformation [47]. Validity of this transformation in the case of corrugated channels has been confirmed by solving both the temporal- and spatial-stability problems and comparing the results.

It is of interest to comment on the possible further evolution of the flow subject to this instability. The growth of traveling waves will likely lead to the formation of finite-amplitude saturation states, as in the case of smooth channel

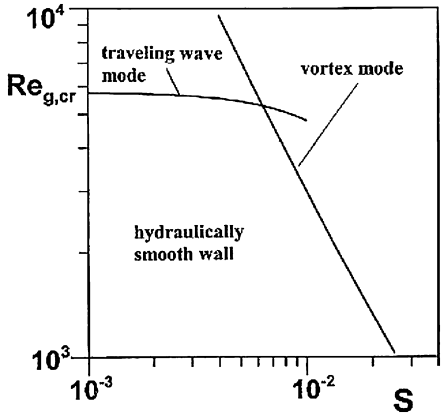

Fig. 20. Variations of the global critical Reynolds number $Re_{g,\mathrm{cr}}$ describing the traveling-wave instability and the vortex-like instability for the wavy-wall corrugation as a function of the corrugation amplitude S for the wavy-wall corrugation. The area below and to the left of both curves corresponds to the flow conditions and the wall geometry that do not produce any instability. Such a wall operating under the specified Reynolds number behaves as a hydraulically smooth wall for this class of corrugation. The global neutral curve for the traveling-wave instability has been taken from [27].

[48–50]. Such states are known to be unstable [51,52] in smooth channels and are likely to remain unstable in the case of corrugated channels.

It is known that the laminar-turbulent transition in two-dimensional Poiseuille flow may occur at Reynolds numbers much lower then those predicted by the unstable eigenvalues of the linear theory. Experiments show that the flow may become turbulent even at $Re = 1000$ [53], which has been recognized as the minimum transition Reynolds number for the channel flow. The presence of corrugation does destabilize the traveling waves, but not to the extent that could explain these observations (Fig. 20). The instability is governed by the non-normal operator [54] and has a subcritical character in the case of smooth walls [55], with the critical Reynolds number reduced to about $Re = 2700$ [48,49]. The operator in the case of corrugated walls consists of a system of Tollmien–Schlichting, Squire- and coupling-like operators connected together by the corrugation effects, as discussed in Section 3, and thus one expect them to be non-normal and the instability to remain subcritical in the case of corrugated walls. The extent of potential corrugation-induced reduction of the non-linear critical Reynolds number is unknown at present.

4.1.3. Global picture for the wavy-wall model

The above discussion shows the existence of two independent modes of instability. Our interest is in identifying flow conditions where the flow is always stable regardless of the form of the corrugation and the type of instability. Fig. 20 displays the critical curves $Re_{g,\mathrm{cr}}(S)$ for both instability modes and permit identification of flow conditions and wall geometry that do not produce any instability. Such wall operating under the specified Reynolds number behaves as the hydraulically smooth wall. The range of Re and S that defines the hydraulically smooth wall is shown in Fig. 20.

The reader should note that the flow conditions outside the "hydraulically smooth" range do not imply flow instability. Flow instability may occur if and only if a particular wall under consideration contains an "active" corrugation wave number. The "hydraulically smooth" conditions guarantee that there is no instability regardless of the corrugation wave number that could be present.

It is necessary here to remind the reader that the laminar-turbulent transition could also be triggered by the so-called transient growth of disturbances [54,56], which could activate nonlinear effects without relying on the asymptotic growth. The transient growth of the wave-like perturbations merely provides a mechanism to increase the level of disturbances required for the flow to jump to a new finite-amplitude state and thus ties back to the question of identification of the structure of the subcritical bifurcation tree. The disturbances with the highest growth, the optimal disturbances, have a form similar to streamwise vortices [57] and lead to the formation of streamwise streaks which, in turn, induce strong secondary instabilities that initiate a route to transition that is not related to subcritical bifurcations. The efficiency of the transient growth in amplifying the disturbances and the form of the optimal disturbances are not known in the case of corrugated wall. One would expect streamwise vortices to remain optimal, albeit with somewhat different characteristics related to the corrugation geometry.

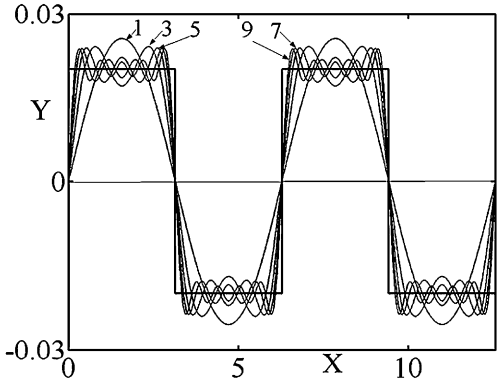

Fig. 21. Rectangular-groove corrugation model. Numbers shown denote the number of Fourier modes retained in Eq. (2.2).

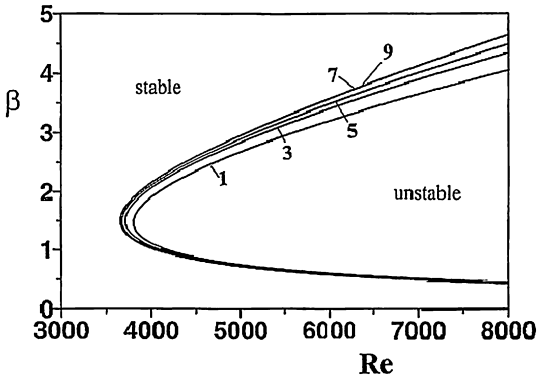

Fig. 22. Neutral curves for the vortex instability in the channel with the rectangular-groove corrugation with the amplitude $S = 0.008$ and the wave number $\alpha = 1$ obtained using various numbers of Fourier modes for the approximation of the corrugation geometry. Numbers shown describe the number of Fourier modes retained in Eq. (2.2).

4.2. Rectangular-groove model

Fig. 21 displays corrugation in the form of rectangular grooves and various geometries obtained with different truncation levels of the Fourier series representing the complete geometry. The Fourier representation has the form given by Eq. (2.2) where $S_0 = 0$, $S_1 = A$, $S_2 = 0$, $S_3 = A/3$, $S_4 = 0$, $S_5 = A/5$, etc., where $A = -4Si/\pi$, $i^2 = -1$ and $4S$ represents the distance between the top and bottom of the corrugation similarly to the case of wavy-wall discussed previously. We begin our discussion with the vortex mode of instability.

Neutral curves for the vortex mode for a typical corrugation geometry with $S = 0.008$ and $\alpha = 1.0$ in the (Re, β) plane are displayed in Fig. 22 for different levels of accuracy of modeling of corrugation geometry. It can be seen that the difference between the critical Reynolds number for the geometries represented by the first seven and nine Fourier modes in Eq. (2.2) (see Fig. 21) is negligible, i.e., the critical conditions for the corrugation in the form of the rectangular groove and the corrugation represented by the first seven Fourier modes are nearly identical. This result demonstrates that the essential properties of the corrugation geometry as far as the flow stability characteristics are concerned can be captured using just a few leading Fourier modes. The reader may also note that the difference between the critical Reynolds numbers for the wavy-wall (one Fourier mode) and the complete geometry is about 4%. It is important to underline that this result shows that the flow is fairly insensitive to small variations of corrugation shape as expressed by higher Fourier modes.

Results of typical parameter studies for the vortex mode carried out with the complete geometry model are shown in Fig. 23. It can be seen that the range of the "active" corrugation wave numbers and the range of the unstable vortices increase with an increase on both Re and S. Qualitative features of this instability are very similar to those observed in the case of wavy-wall (see Section 4.1.1) while the details are obviously somewhat different. An extreme sensitivity of the instability with respect to the amplitude of the corrugation as well as the Reynolds number once critical conditions are reached is noted. Numerous repetitions of studies similar to those displayed in Fig. 23 permit identification of the global critical conditions as a function of the corrugation amplitude S. The global critical Reynolds numbers $Re_{g,\mathrm{cr}}$, the global critical corrugation wave numbers $\alpha_{g,\mathrm{cr}}$ and the global critical vortex wave numbers $\beta_{g,\mathrm{cr}}$ displayed in Fig. 24 demonstrate that their variations as a function of S are qualitatively similar to the case of wavy-wall. The critical curve is almost exactly parallel to the corresponding curve for the wavy-wall; it appears to be just shifted downwards by a constant distance in the $(\log(Re_{g,\mathrm{cr}}), \log(S))$ plane. The global critical Reynolds number $Re_{g,\mathrm{cr}}$ is lower by about 20% as compared to the $Re_{g,\mathrm{cr}}$ for the wavy-wall with the same amplitude, while $\alpha_{g,\mathrm{cr}}$ is about 15% lower and $\beta_{g,\mathrm{cr}}$ is nearly identical. We may conclude by looking at the shape of the corrugation shown in Fig. 21 that the flow destabilization as compared to the wavy-wall case is owing to the presence of higher Fourier modes in the corrugation shape.

We shall now turn our attention to the traveling wave mode. Results shown in Fig. 25 demonstrate the variations of the neutral curve in the (δ, Re) plane as a function of different approximations of the corrugation geometry expressed

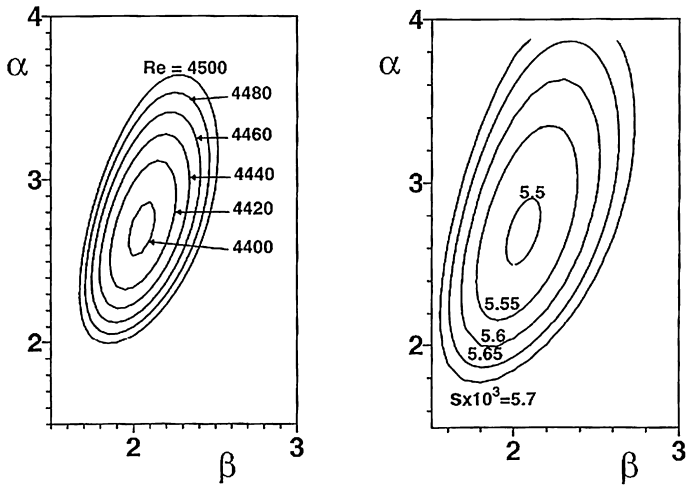

Fig. 23. Neutral stability curves for the vortex instability in the channel with the rectangular-groove corrugation. A – effects of the flow Reynolds number Re for the corrugation amplitude $S = 0.0056$; B – effects of the corrugations amplitude S for the flow Reynolds number $Re = 4500$.

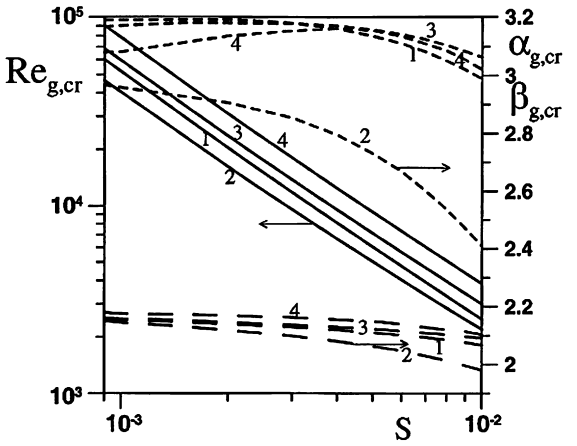

Fig. 24. Variations of the global critical stability conditions, i.e., $Re_{g,\mathrm{cr}}$, $\alpha_{g,\mathrm{cr}}$ and $\beta_{g,\mathrm{cr}}$, for disturbances in the form of streamwise vortices. The solid, short-dash and long-dash lines refer to $Re_{g,\mathrm{cr}}$, $\alpha_{g,\mathrm{cr}}$ and $\beta_{g,\mathrm{cr}}$, respectively. Labels 1, 2, 3 and 4 refer to the corrugation in the form of wavy wall, rectangular grooves, triangular grooves and "sine-bump" grooves, respectively.

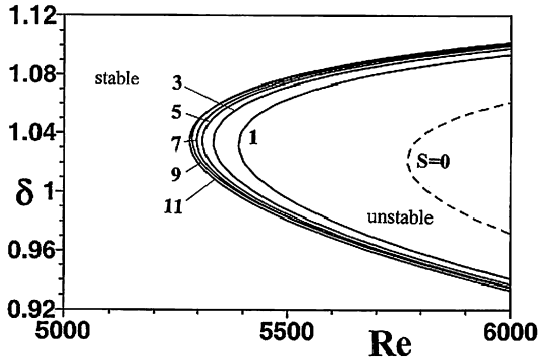

Fig. 25. Neutral curves for the traveling-wave instability in the channel with the rectangular-groove corrugation with the amplitude $S = 0.006$ and wave number $\alpha = 1$ obtained using various numbers of Fourier modes for the approximation of the corrugation geometry. Numbers shown describe the number of Fourier modes retained in Eq. (2.2). Dash line shows neutral curve for the smooth wall.

in terms of different levels of truncation of Fourier expansion (2.2). It can be seen that the critical Reynolds numbers for the geometries represented by the nine-modes and eleven-modes Fourier expansions are nearly identical. The difference between the critical Reynolds number for the complete geometry and for the wavy-wall model is of the order of 2%.

Results of typical parameter studies for the traveling wave mode are illustrated in Fig. 26. The qualitative character of the flow response is very similar to the case of wavy-wall (see Section 4.1.2). The global critical Reynolds numbers $Re_{g,\mathrm{cr}}$, the global critical corrugation wave numbers $\alpha_{g,\mathrm{cr}}$ and the global critical vortex wave numbers $\delta_{g,\mathrm{cr}}$ for this type of instability are displayed in Fig. 27 and demonstrate qualitative similarity with the wavy-wall case. The global critical Reynolds number for the grooved wall is lower by about 5% as compared with the wavy-wall case for the largest corrugation amplitude considered, while the global critical corrugation wave number $\alpha_{g,\mathrm{cr}}$ is nearly 50%

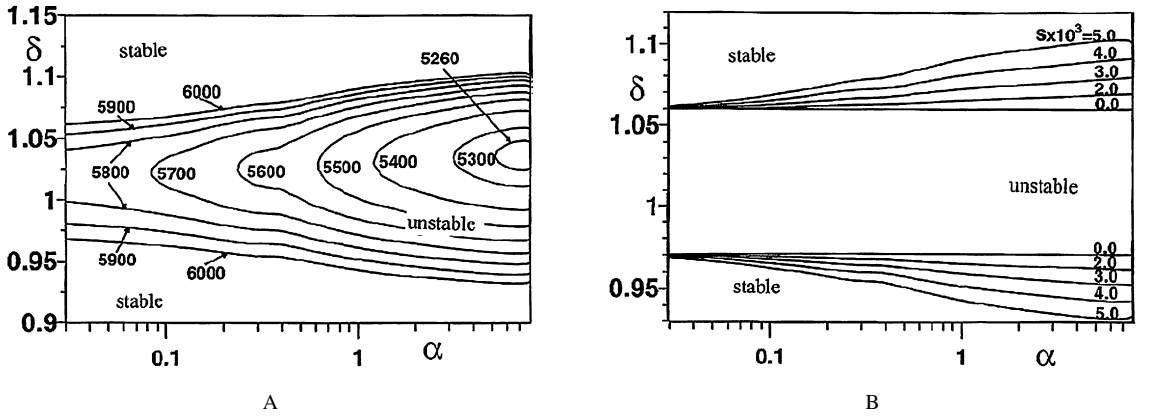

Fig. 26. Neutral stability curves for the traveling-wave instability in the channel with the rectangular-groove corrugation. A – effects of the flow Reynolds number Re for the corrugation amplitude $S = 0.005$; B – effects of the corrugations amplitude S for the flow Reynolds number $Re = 6000$.

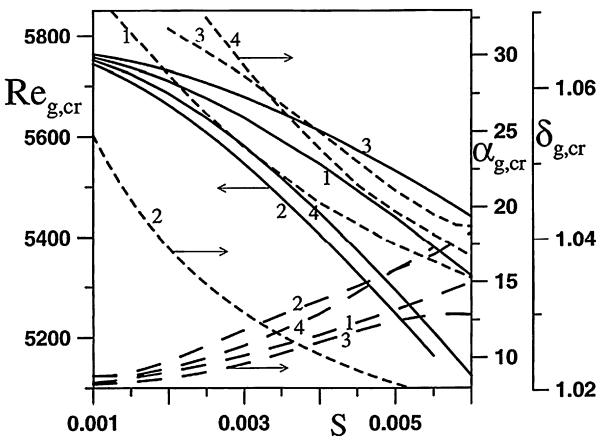

Fig. 27. Variations of the global critical stability conditions, i.e., $Re_{g,\mathrm{cr}}$, $\alpha_{g,\mathrm{cr}}$ and $\delta_{g,\mathrm{cr}}$, for disturbances in the form of traveling waves. The solid, short-dash and long-dash lines refer to $Re_{g,\mathrm{cr}}$, $\alpha_{g,\mathrm{cr}}$ and $\delta_{g,\mathrm{cr}}$, respectively. Labels 1, 2, 3 and 4 refer to the corrugation in the form of wavy wall, rectangular grooves, triangular grooves and "sine-bump" grooves, respectively. The reader may note that $Re_{g,\mathrm{cr}} \to 5772$ and $\delta_{g,\mathrm{cr}} \to 1.02$ as $S \to 0$.

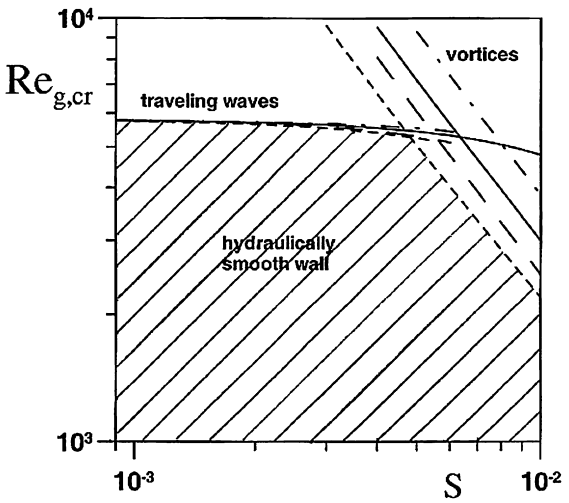

Fig. 28. Variations of the global critical Reynolds number $Re_{g,\mathrm{cr}}$ describing the traveling-wave instability and the vortex-like instability for the corrugated channel as a function of the corrugation amplitude S. The dash, dash-dot and continuous lines correspond to the corrugation in the form of rectangular grooves, triangular grooves and "sine-bump" grooves, respectively. The shaded area corresponds to the flow conditions that do not produce any instability for the corrugation geometries subject to this investigation.

smaller over the whole range of corrugation amplitudes considered (Fig. 27). The critical wave number $\delta_{g,\mathrm{cr}}$ is nearly identical in both cases. We can conclude again that higher Fourier modes are responsible for the flow destabilization.

Analysis of results for the vortex and traveling wave modes presented above permits formulation of the global picture of the instability. Fig. 28 displays the global critical curves for both modes. The region below these curves identifies conditions under which the wall with the rectangular grooves behaves as a hydraulically smooth wall. The flow is less stable than the flow over a wavy-wall with the same amplitude.

4.3. Triangular-groove model

Figure 29 illustrates corrugation in the form of triangular grooves and various geometries obtained with different truncation levels of the Fourier series representing the complete geometry. The Fourier representation has the form given by Eq. (2.2) where $S_0 = 0$, $S_1 = A$, $S_2 = 0$, $S_3 = 3^{-2}A$, $S_4 = 0$, $S_5 = 5^{-2}A$, etc., where $A = -8S/\pi^2$ and

4S represents the distance between the top and bottom of the corrugation. It had been found that in most cases the stability characteristics for the triangular grooves and the corrugation shape described by the first three modes of Fourier expansion (2.2) were nearly identical.

We begin discussion with the vortex mode. Results of typical parameter studies are shown in Fig. 30. The qualitative features of this instability are very similar to those observed in the previous two cases. An extreme sensitivity of the instability with respect to the amplitude of the corrugation as well as the flow Reynolds number once critical conditions are reached is noted. The global critical Reynolds numbers $Re_{g,\mathrm{cr}}$, the global critical corrugation wave numbers $\alpha_{g,\mathrm{cr}}$ and the global critical vortex wave numbers $\beta_{g,\mathrm{cr}}$ displayed in Fig. 24 demonstrate that their variations as a function of S are qualitatively similar to the previous two cases, i.e., wavy-wall model and rectangular-groove model. The $Re_{g,\mathrm{cr}}$ is parallel to the similar curve for the wavy-wall and is just shifted upwards resulting in a more stable flow. The global critical Reynolds number $Re_{g,\mathrm{cr}}$ is higher by about 10% as compared with the wavy-wall case, while $\alpha_{g,\mathrm{cr}}$ and $\beta_{g,\mathrm{cr}}$ are nearly identical. The first Fourier mode in the corrugation shape corresponds to the wavy-wall with smaller amplitude (see Fig. 29) and this is why this flow is more stable as compared with the wavy-wall with the same amplitude as triangular grooves; the higher Fourier modes in the corrugation shape are not effective in flow

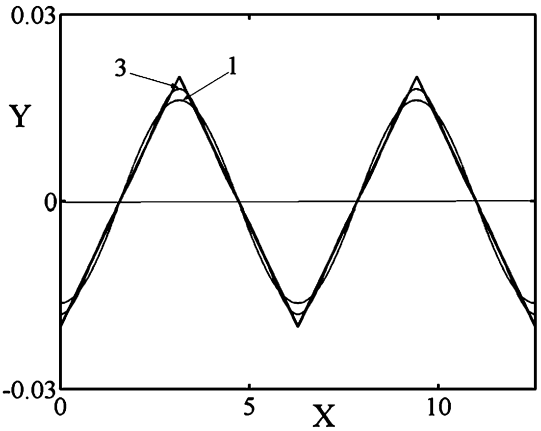

Fig. 29. Triangular-groove corrugation model. Numbers shown denote the number of Fourier modes retained in Eq. (2.2).

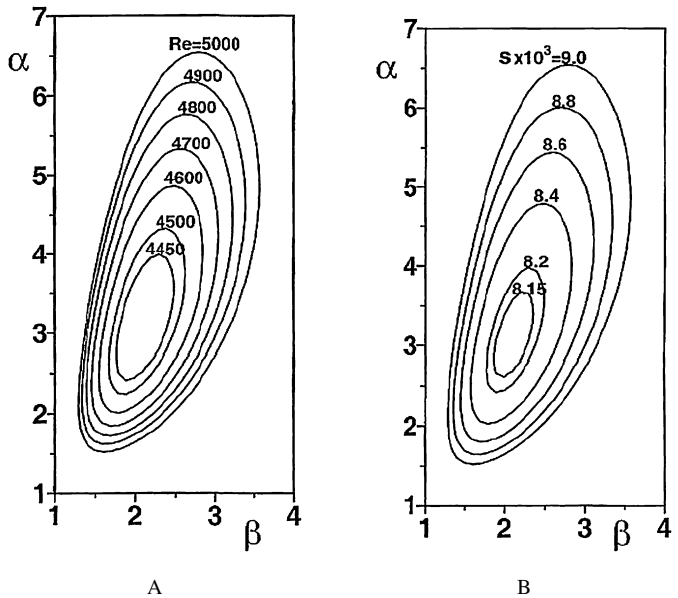

Fig. 30. Neutral stability curves for the vortex instability in the channel with the triangular-groove corrugation. A – effects of the flow Reynolds number Re for the corrugation amplitude $S = 0.009$; B – effects of the corrugations amplitude S for the flow Reynolds number $Re = 5000$.

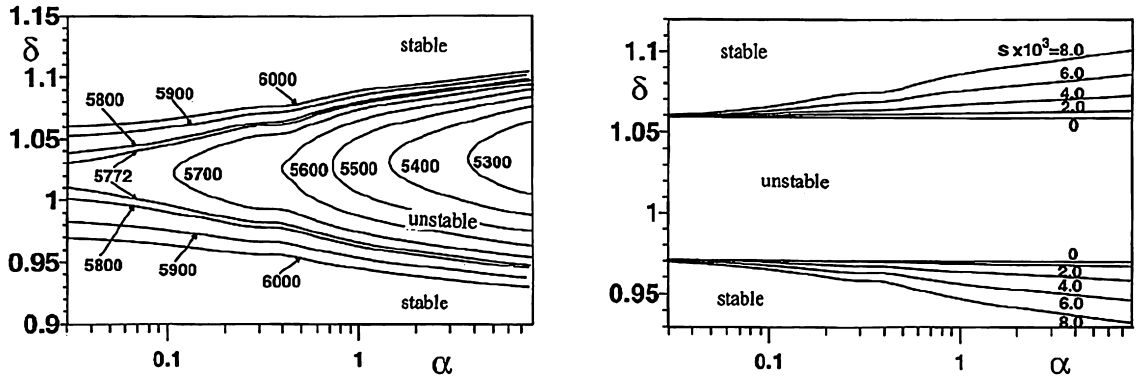

Fig. 31. Neutral stability curves for the traveling-wave instability in the channel with the triangular-groove corrugation. A – effects of the flow Reynolds number Re for the corrugation amplitude $S = 0.0085$; B – effects of the corrugations amplitude S for the flow Reynolds number $Re = 6000$.

destabilization. Accordingly, we can conclude that the $Re_{g,\mathrm{cr}}$ curve is shifted towards higher S as compared to the wavy-wall case rather than towards higher $Re_{g,\mathrm{cr}}$. The net result is obviously the same, regardless of the interpretation adopted.

We shall now turn our attention to the traveling wave mode. Results of typical parameter studies are illustrated in Fig. 31. The qualitative character of the flow response is very similar to the previous two cases. The global critical Reynolds numbers $Re_{g,\mathrm{cr}}$, the global critical corrugation wave numbers $\alpha_{g,\mathrm{cr}}$ and the global critical vortex wave numbers $\delta_{g,\mathrm{cr}}$ for this type of instability are displayed in Fig. 27 and demonstrate qualitative similarity with the wavy-wall and rectangular-groove cases. The flow over the triangular grooves is least unstable from among the cases studied so far, with $Re_{g,\mathrm{cr}}$ higher by about 5% as compared to the wavy-wall case at the highest value of S considered; $\alpha_{g,\mathrm{cr}}$ and $\delta_{g,\mathrm{cr}}$ are nearly the same as in the wavy-wall case. The reason for flow stabilization relative to the wavy-wall is the same as in the case of vortex instability, i.e., the dominant mode in the corrugation shape corresponds to the wavy-wall with a smaller amplitude.

The above discussion permits formulation of the global picture of the instability. Fig. 28 displays the global critical curves for the vortex and traveling-wave modes. The region below these curves identifies conditions under which the wall with the triangular grooves behaves as a hydraulically smooth wall. This flow is more stable than the wavy-wall case.

4.4. "Sine-bump"-groove model

Fig. 32 illustrates corrugation in the form of "sine-bump" grooves and various geometries obtained with different truncation levels of the Fourier series representing the complete geometry. The groove is made out of straight line extending over half of a period and half period of sine function. The Fourier representation has the form given by Eq. (2.2) where $S_0 = 0$, $S_1 = -2S\mathrm{i}$, $S_2 = A/(1*3)$, $S_3 = 0$, $S_4 = A/(3*5)$, $S_5 = 0$, $S_6 = A/(5*7)$, etc., where $A = -8/\pi$, $\mathrm{i}^2 = -1$ and $4S$ represents the distance between the top and bottom of the corrugation. It had been found that the stability characteristics for the "sine-bump" grooves and the corrugation shape described by the first three modes of the Fourier expansion (2.2) were nearly identical.

We shall begin our discussion with the vortex mode. Results of typical parameter studies are shown in Fig. 33. The qualitative features of this instability are very similar to those observed in the previous three cases. The $Re_{g,\mathrm{cr}}$, the $\alpha_{g,\mathrm{cr}}$ and the $\beta_{g,\mathrm{cr}}$ displayed in Fig. 24 demonstrate that their variations as a function of S are qualitatively similar in all cases studied so far. This flow is actually more stable than the triangular-groove case (and thus more stable than the wavy-wall case), which is probably because of the greater dominance of the first Fourier mode in the corrugation shape (Fig. 32).

We shall now turn our attention to the traveling wave mode. Results of typical parameter studies are illustrated in Fig. 34. The qualitative character of the flow response is very similar to the previous three cases. The $Re_{g,\mathrm{cr}}$, the $\alpha_{g,\mathrm{cr}}$ and the $\delta_{g,\mathrm{cr}}$ for this type of instability are not too far away from the corresponding values for the wavy-wall, as

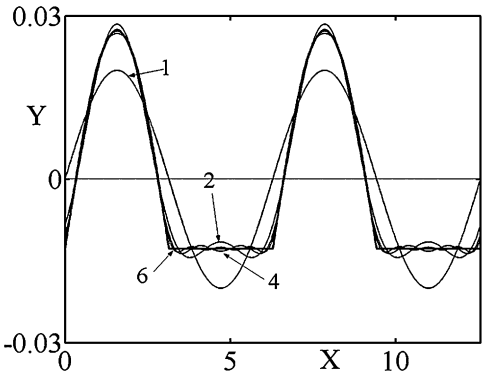

Fig. 32. "Sine-bump"-groove corrugation model. Numbers shown denote the number of Fourier modes retained in Eq. (2.2).

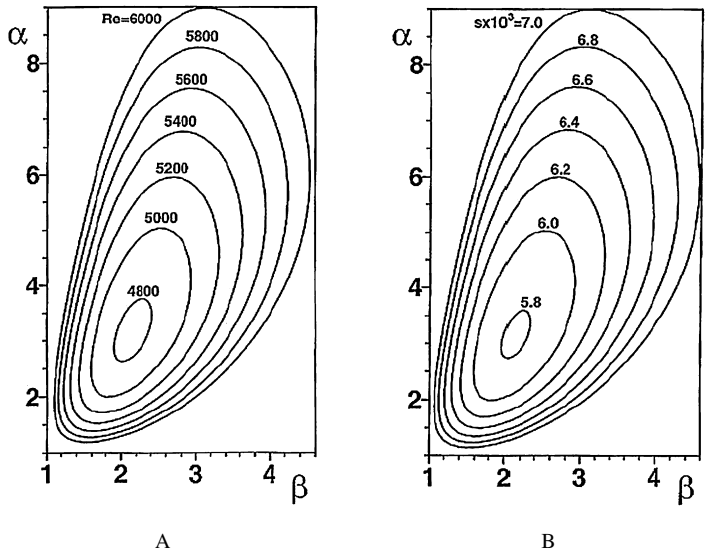

Fig. 33. Neutral stability curves for the vortex instability in the channel with the "sine-bump"-groove corrugation. A – effects of the flow Reynolds number *Re* for the corrugation amplitude $S = 0.009$; B – effects of the corrugations amplitude *S* for the flow Reynolds number $Re = 5000$.

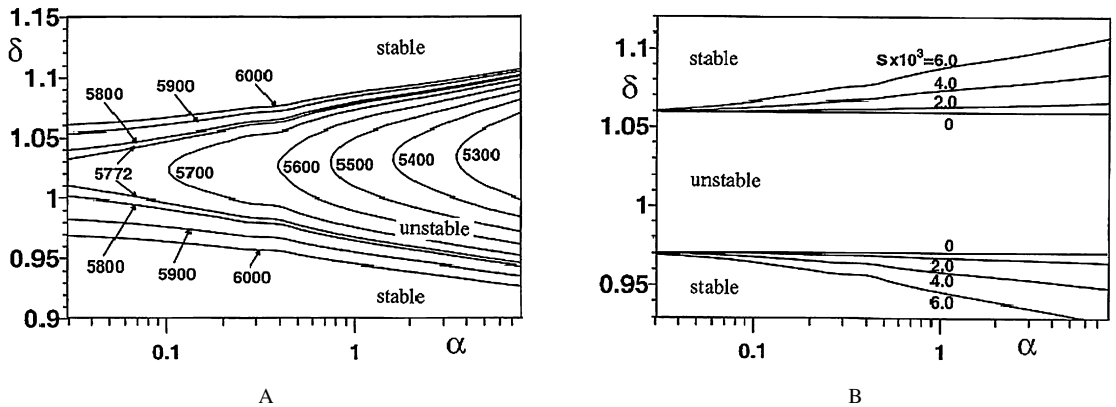

Fig. 34. Neutral stability curves for the traveling-wave instability in the channel with the "sine-bump"-groove corrugation. A – effects of the flow Reynolds number *Re* for the corrugation amplitude $S = 0.0085$; B – effects of the corrugations amplitude *S* for the flow Reynolds number $Re = 6000$.

demonstrated in Fig. 27, and illustrate qualitative similarity of all cases studied so far. The reader may note that this flow is actually less stable with respect to traveling waves than the wavy-wall case.

The global picture of the instability is illustrated in Fig. 28, which displays the global critical curves for both modes. The region below these curves identifies conditions under which the wall with the "sine-bump"-grooves behaves as a hydraulically smooth wall. This wall falls in between the wavy-wall and the rectangular-groove cases as far as traveling-wave instability is concerned but is the most stable as far as the vortex instability is concerned.

5. Comparison of dynamical effect induced by different classes of corrugation shapes and closing comments

Results described above for the four corrugation shapes permit us to draw fairly general conclusions regarding linear instability of the two-dimensional channel flow bounded by a corrugated wall. The wavy-wall has been selected as the reference case as its shape is represented by a single Fourier mode. The rectangular grooves have been selected to represent the most extreme geometry that can be represented using Fourier series; in this case higher Fourier modes play significant part in representing the corrugation shape (see Fig. 21). Triangular grooves have been selected to represent shapes where higher Fourier modes do not play a significant role (see Fig. 29). The "sine-bump" model has been selected to represent a mixed case between the wavy-wall and the rectangular and triangular grooves (see Fig. 32). The more complex shapes with grooves folding onto themselves are probably of no significance as the flow separation would effectively "smooth out" the geometry and the free shear layers around the top of the small separation bubbles would probably be too short to support any local instabilities and the local Reynolds number would probably be too small to permit growth of any disturbances.

The critical curves displayed in Fig. 28 demonstrate qualitative similarity of flow response for all corrugation geometries subject to this investigation. If the corrugation amplitude for a given shape and distribution (as defined by the corrugation wave number) and given flow conditions (as defined by the flow Reynolds number) is sufficiently small, such corrugation is able to induce only small modifications in the flow. When the size of the corrugation reaches critical conditions, it can induce large changes in the flow through various instability processes. We can therefore use the onset of any instability as the event that defines the conditions when the wall ceases to be hydrodynamically smooth.

The flow is subject to two types of instability. The traveling-wave instability has its critical Reynolds number always reduced by the presence of the corrugation. The corrugation is always able to initiate a new instability that results in the formation of streamwise vortices. The similarity of the flow response for all geometries studied is especially clear in the case of vortex instability, where the critical curves are just shifted by a constant distance in the $(\log(Re_{g,\mathrm{cr}}), \log(S))$ plane. The remarkable fact is that the quantitative results are also very similar for all geometries considered. The wavy-wall model provides a surprisingly good approximation for all corrugation shapes in the case of traveling-wave instability; the spread of $Re_{g,\mathrm{cr}}$ for the same amplitude but different corrugation shapes is of the order of 5% of the wavy-wall value for the largest amplitude S considered. The spread of $Re_{g,\mathrm{cr}}$ for the vortex instability is of the order of 60% of the wavy-wall value over the whole range of amplitudes S considered; however, the wavy-wall value under-predicts $Re_{g,\mathrm{cr}}$ for the most dangerous shape (rectangular grooves) by only 20%. The traveling waves are fairly insensitive to the corrugation shape and corrugation amplitude, while the vortices are very sensitive to both. The rectangular grooves, which represent the most extreme geometry, are found to be the most effective in flow destabilization. Since more complex shapes, with grooves folding onto themselves, are likely to be "smoothed out" by the flow separation as argued above, the results for the rectangular grooves permit us to identify the flow conditions and corrugation amplitudes where the wall with surface corrugation always would behave as hydraulically smooth wall regardless of the corrugation shape (see Fig. 28). An increase of Re above its maximum permitted hydraulically-smooth-value induces traveling-wave instability if the corrugation amplitude $S \leqslant \sim 0.0045$, and vortex instability for larger values of S. The reader should keep in mind that the flow becomes unstable for $Re > Re_{g,\mathrm{cr}}$ only if the given corrugation shape contains hydraulically "active" corrugation wave numbers.

The reader may recall that our interest is in the determination of the effects of distributed surface roughness. In the analysis we have considered a number of carefully selected corrugations and were able to formulate conclusions valid regardless of details of their shapes. The generality of these results permits us to return to the use of the term "roughness" and conclude that any rough wall is hydraulically smooth as long as it does not induce any instability. Obviously, this conclusion applies to transitional flows only, as different effects not accounted for in the present analysis may play a role in the case of turbulent flows.

The results summarized above have been obtained in the case of two-dimensional roughness shapes. Variations of the roughness geometry in the spanwise direction are likely to introduce new instability mechanisms and have to be studied separately. The hydraulically smooth wall, as defined above, remains therefore hydraulically smooth if and only if the surface roughness has the form of spanwise grooves.

Acknowledgements

This work has been carried out with support of NSERC of Canada. The author would like to thank Dr.S.Krol for assistance in carrying out the required computations. Sharcnet of Canada provided computing resources.

Appendix A

Operators used in Eqs. (3.5) have the following definitions [26,29]:

$$S^{(m)} = D^2 - k_m^2 - \mathrm{i}Re(t_m u_0 - \sigma), \tag{A.1}$$

$$T^{(m)} = \left(D^2 - k_m^2\right)^2 - \mathrm{i}Re\left[(t_m u_0 - \sigma)\left(D^2 - k_m^2\right) - t_m D^2 u_0\right], \tag{A.2}$$

$$C = Re\beta D u_0, \tag{A.3}$$

$$W_u^{(m,n)} = \beta\left(\mathrm{i} f_v^{(n)} D - t_m f_u^{(n)}\right), \tag{A.4}$$

$$W_v^{(m,n)} = \mathrm{i}\beta D f_u^{(n)}, \tag{A.5}$$

$$W_w^{(m,n)} = t_m\left(t_{m-n} f_u^{(n)} - i f_v^{(n)} D\right), \tag{A.6}$$

$$B_u^{(m,n)} = -t_m^2 D f_u^{(n)} + \mathrm{i}n\alpha k_m^2 f_v^{(n)} - t_m^2 f_u^{(n)} D + \mathrm{i}t_m D f_u^{(n)} D + \mathrm{i}t_m f_v^{(n)} D^2, \tag{A.7}$$

$$B_v^{(m,n)} = \mathrm{i}k_m^2 t_{m-n} f_u^{(n)} + k_m^2 D f_v^{(n)} + k_m^2 f_v^{(n)} D + \mathrm{i}t_m D^2 f_u^{(n)} + \mathrm{i}t_m D f_u^{(n)} D, \tag{A.8}$$

$$B_w^{(m,n)} = \beta\left(-t_{m-2n} f_u^{(n)} D - t_{m-n} D f_u^{(n)} + \mathrm{i} f_v^{(n)} D^2\right), \tag{A.9}$$

where $D = d/dy$ and $k_m^2 = t_m^2 + \beta^2$.

References

[1] G. Hagen, Über den Einfluss der Temperatur auf die Bewegung des Wasser in Röhren, Math. Abh. Akad. Wiss., Berlin, (1854) 17–98.
[2] H. Darcy, Recherches expérimentales relatives au mouvement de l'eau dans les tuyaux, Mallet-Bachelier, Paris, 1857.
[3] O. Reynolds, An experimental investigation of the circumstances which determine whether the motion of water shall be direct or sinuous, and of the wall of resistance in parallel channels, Philos. Trans. Roy. Soc. London 174 (1883) 935–982.
[4] J. Jimenez, Turbulent flows over rough walls, Annu. Rev. Fluid Mech. 36 (2004) 173–196.
[5] J. Nikuradse, Strömungsgesetze in Rauhen Rohren, VDI-Forschungscheft #361 (1933); also NACA TM 1292 (1950).
[6] C.F. Colebrook, Turbulent flow in pipes, with particular reference to the transition region between the smooth and rough pipes, J. Inst. Civil Engineers London 11 (1939) 133–156.
[7] L.F. Moody, Friction factors for pipe flow, Trans. ASME 66 (1944) 671–684.
[8] P. Bradshaw, A note on "critical roughness" and "transitional roughness", Phys. Fluids 12 (2000) 1611–1614.
[9] D.R. Waigh, R.J. Kind, Improved aerodynamic characterization of regular three-dimensional roughness, AIAA J. 36 (1998) 1117–1119.
[10] M.V. Morkovin, On roughness-induced transition: facts, views and speculations, in: M.Y. Hussaini, R.G. Voigt (Eds.), Instability and Transition, in: ICASE/NASA LARC Series, vol. 1, Springer, 1990, pp. 281–295.
[11] A. Fage, The smallest size of spanwise surface corrugation which affects boundary layer transition on an airfoil, Br. Aero. Res. Council Report No. 2120, 1943.
[12] B.H. Carmichael, Surface waviness criteria for swept and unswept laminar suction wings, Northrop Aircraft Report No. NOR-59-438 (BLC123), 1957.
[13] H. Schlichting, Boundary Layer Theory, seventh ed., McGraw-Hill, 1979.
[14] I. Tani, Effect of two dimensional and isolated roughness elements, in: G.V. Lachman (Ed.), Boundary Layer and Flow Control, vol. 2, Pergamon, 1961, pp. 637–656.
[15] A.E. Doenhoff, A.L. Braslow, The effect of distributed surface roughness on laminar airfoil, in: G.V. Lachman (Ed.), Boundary Layer and Flow Control, vol. 2, Pergamon, 1961, pp. 657–681.
[16] P.S. Klebanoff, K.D. Tidstrom, Mechanism by which a two-dimensional roughness element induces boundary layer transition, Phys. Fluids 15 (1972) 1172–1188.
[17] A.H. Nayfeh, S.A. Ragab, A.A. Al-Maaitah, Effect of bulges on the stability of boundary layers, Phys. Fluids 4 (1988) 796–806.
[18] J.A. Masad, V. Iyer, Transition prediction and control in subsonic flow over a hump, Phys. Fluids 6 (1994) 313–327.

[19] J.M. Floryan, On the Görtler instability of boundary layers, Progr. Aerospace Sci. 28 (1991) 235–271.
[20] E. Reshotko, Disturbances in a laminar boundary layer due to distributed surface roughness, in: T. Tatsumi (Ed.), Turbulence and Chaotic Phenomena, Proceedings of IUTAM Symposium, Elsevier, 1984, pp. 39–46.
[21] T.C. Corke, A. Bar Sever, M.V. Morkovin, Experiments on transition enhancements by distributed roughness, Phys. Fluids 29 (1986) 3199–3213.
[22] K. Singh, J.L. Lumley, Effect of roughness on the velocity profile of a laminar boundary layer, Appl. Sci. Res. 24 (1972) 168–186.
[23] M. Lessen, S.T. Gangwani, Effect of small amplitude wall waviness upon the stability of the laminar boundary layer, Phys. Fluids 19 (1976) 510–513.
[24] J.M. Kendall, Laminar boundary layer velocity distortion by surface roughness: Effect upon stability, AIAA Paper 81-0195, AIAA 19th Aerospace Sciences Meeting, 1981.
[25] C.L. Merkle, K.T.-S. Tzou, T. Kubota, An analytical study of the effect of surface roughness on boundary layer stability, Dynamics Technology Inc., Report DT-7606-4, 1977.
[26] J.M. Floryan, Stability of wall-bounded shear layers in the presence of simulated distributed roughness, J. Fluid Mech. 335 (1997) 29–55.
[27] J.M. Floryan, Two-dimensional instability of flow in a rough channel, Phys. Fluids 17 (2005) 044101/8.
[28] J.M. Floryan, M. Asai, Stability of flow in a rough channel, in: Proceedings of the 21 International Congress of Theoretical and Applied Mechanics, Warsaw, Poland, Springer, 2004.
[29] J.M. Floryan, Centrifugal instability of Couette flow over a wavy-wall, Phys. Fluids 14 (2002) 312–322.
[30] J.M. Floryan, Vortex instability in a converging-diverging channel, J. Fluid Mech. 482 (2003) 17–50.
[31] E. Reshotko, A. Tumin, Investigation of the role of transient growth in roughness induced transition, AIAA Paper 2002-2850, 32nd AIAA Fluid Dynamics Conference, St. Louis, 2002.
[32] J. Szumbarski, J.M. Floryan, A direct spectral method for determination of flows over corrugated boundaries, J. Comp. Phys. 153 (1999) 378–402.
[33] W.R.C. Phillips, On the nonlinear instability of strong wavy shear to longitudinal vortices, in: L. Debnath, D.N. Riahi (Eds.), Nonlinear Instability, Chaos and Turbulence, in: Advances in Fluid Mechanics, vol. 20, WIT Press, UK, 1999, pp. 251–273.
[34] Lord Rayleigh, On the dynamics of the revolving fluids, Scientific Papers 6 (1920) 447–453.
[35] H.B. Squire, On the stability of three-dimensional disturbances of viscous flow between parallel walls, Proc. Roy. Soc. A 142 (1933) 621–628.
[36] W.M. Orr, The stability or instability of the steady motions of a perfect liquid and a viscous liquid, Proc. Roy. Irish Acad. A 27 (1907) 9–27, 69–138.
[37] A. Sommerfeld, Ein Beitrag zur hydrodynamishen Erklärung der turbulenten Flüssigkeitsbewegung, in: Proceedings of the 4th International Congress of Mathematicians, III, Roma, 1908, pp. 116–124.
[38] L.M. Mack, A numerical study of the temporal eigenvalue spectrum of the Blasius boundary layer, J. Fluid Mech. 73 (1976) 497–520.
[39] A.E. Perry, B.D. Fairlie, Critical points in flow patterns, Adv. Geophys. B 18 (1974) 299–315.
[40] J.M. Floryan, Görtler instability of boundary layers over concave and convex walls, Phys. Fluids 29 (1986) 2380–2387.
[41] A.D.D. Craik, Wave-induced longitudinal-vortex instability in shear flows, J. Fluid Mech. 125 (1982) 37–82.
[42] S. Leibovich, Convective instability of stably stratified water in the ocean, J. Fluid Mech. 82 (1977) 561–585.
[43] J.H.M. Fransson, A. Talamelli, L. Brandt, C. Cossu, Delaying transition to turbulence by a passive mechanism, Phys. Rev. Lett. 96 (2006) 064501.
[44] T. Cabal, J. Szumbarski, J.M. Floryan, Stability of flow in a wavy channel, J. Fluid Mech. 457 (2002) 191–212.
[45] W. Tollmien, Ein allgemeines Kriterium der Instabilität laminarer Geschwindigkeitsverteilungen, Nachrichten von der Gesellschaft der Wissenschafen zu Göttingen, Mathematisch-Physische Klasse, Fachgruppe I 1 (1935) 79–114 (also: General instability criterion of laminar velocity distributions, National Advisory Committee for Aeronautics, Washington, Technical Memorandum No. 792 (1936)).
[46] H. Schlichting, Berechnung der Anfachung kleiner Störungen bei der Plattenströmung, ZAMM 13 (1933) 171–174.
[47] M. Gaster, A note on the relation between temporally-increasing and spatially-increasing disturbances in the hydrodynamic stability theory, J. Fluid Mech. 14 (1962) 222–224.
[48] T. Herbert, Finite amplitude stability of plane parallel flows, AGARD Conf. Proc. 224 (1977) 3.1–3.10.
[49] U. Ehrenstein, W. Koch, Three-dimensional wavelike equilibrium states in plane Poiseuille flow, J. Fluid Mech. 228 (1991) 111–148.
[50] J. Jimenez, Transition to turbulence in two-dimensional Poiseuille flow, J. Fluid Mech. 218 (1990) 265–297.
[51] S.A. Orszag, A.T. Patera, Secondary instability of wall-bounded shear flows, J. Fluid Mech. 128 (1983) 347–385.
[52] T. Herbert, Secondary instability of boundary layers, Annu. Rev. Fluid Mech. 20 (1988) 487–526.
[53] M. Nishioka, M. Asai, Some observations of the subcritical transition in plane Poiseuille flow, J. Fluid Mech. 150 (1985) 441–450.
[54] L.N. Trefethen, A.E. Trefethen, S.C. Reddy, T.A. Driscoll, Hydrodynamic stability without eigenvalues, Science 261 (1993) 577–584.
[55] J.T. Stuart, On the non-linear mechanics of wave disturbances in stable and unstable parallel flows. Part 1. The basic behavior in plane Poiseuille flow, J. Fluid Mech. 9 (1960) 353–370.
[56] S.C. Reddy, P.J. Schmid, D.S. Henningson, Pseudospectra of the Orr–Sommerfeld operator, SIAM J. Appl. Math. 53 (1993) 15–47.
[57] K.M. Butler, B.F. Farrell, Three-dimensional optimal perturbations in viscous shear flow, Phys. Fluids A 4 (1992) 1637–1650.